ISSN 0509-6669

TRANSACTIONS OF THE INSTITUTE OF AVIATION

Scientific Quarterly
1/2009 (196)

REVIEW OF AERONAUTICAL FATIGUE INVESTIGATIONS IN POLAND DURING THE PERIOD MAY 2007 TO APRIL 2009

Antoni Niepokólczycki, DSc, Editor

Edition is sponsored by Ministry of Science and Higher Education

ТРУДЫ ИНСТИТУТА АВИАЦИИ

НАУЧНОЙ ЖУРНАЛ (КВАРТАЛНИК)

1/2009 (196)

ОБЗОР АВИАЦИОННЫЫХ УСТАЛОСТНЫХ РАССЛЕДОВАНИИ В ПОЛЬШЕ В ПЕРИОД С МАЯ 2007 ПО АПРЕЛЬ 2009

Редактор: др Антони Непокулчыцки

Publisher: Institute of Aviation
Scientific Publicatins Group
Al. Krakowska 110/114 02-256 Warszawa, Poland
phone: (4822) 846 00 11 ext 442, fax: (4822) 846 44 32
Edition, revision, computer typesetting: Tadeusz Korsak
Printers: ALKOR, 05-070 Sulejówek, Krucza 4

CONTENTS

СОДЕРЖАНИЕ

1. INTRODUCTION

This review gives the summary of work performed in Poland in the area of aeronautical fatigue during the period from May 2007 to April 2009.

The various contributions to this review come from the following sources:

Institute of Aviation, Warsaw;

Air Force Institute of Technology, Warsaw;

Warsaw University of Technology, Warsaw;

Military University of Technology, Warsaw;

AGH University of Science and Technology, Cracow;

Rzeszow University of Technology, Rzeszow;

PZL ŚWIDNIK, Świdnik;

PZL MIELEC, Mielec.

The names of the principal investigators and their affiliations are presented in brackets at the end of each topic title.

Full addresses of contributors are available through the author of this review at:

Antoni NIEPOKÓLCZYCKI
Institute of Aviation
Al. Krakowska 110/114
02-256 Warsaw, POLAND
Phone: (+48-22) 846 08 01 ext. 546
Fax: (+48-22) 846 44 32
E-mail: antekn@ilot.edu.pl

2. HELICOPTERS

2.1 Static, Fatigue and Durability Tests of Main and Tail Rotor Gearboxes of PZL SW-4 Helicopter

(Marek Stawski – PZL ŚWIDNIK)

PZL Swidnik is the main Polish producer of helicopters with over 50 year tradition. The main models of the helicopter manufactured in Swidnik are PZL- Falcon and PZL SW-4.

The PZL SW-4 is a single turbine, light multipurpose helicopter designed to carry up to 5 persons including pilot(s) under day and night VFR. The helicopter has a conventional rotor system and is powered by a single Rolls-Royce 250 C20-R/2(SP) engine (336kW, 450shp, 457 Metric hp). Helicopter is designed for compliance with FAR-27 (through amendment 27- 33) and JAR-27 regulations.

The first casings of main and tail gearboxes for SW-4 were produced at WSK Rzeszow. They were made from GA8 magnesium alloy. However, PZL Swidnik took over this production from WSK Rzeszow and decided to exchange the material of the casings for the AlSiMg0.6 alloy. So, the producer has to perform static, fatigue and durability tests for both main and tail gearboxes, whose casings are made from both magnesium and aluminium alloys.

First, the fatigue tests of specimens made from both alloys were performed in order to compare the fatigue strength of these alloys. The conclusion drawn from these tests is the average fatigue strength of AlSiMg0.6 alloy is at least 65% higher than that of GA8 alloy.

Second, the static tests of both casings were performed. Both casings successfully withstood static load equal to 250% of safe load.

Now, the fatigue tests of both gearboxes are being carried out. Three casings of each type will be investigated. Now, April 2009, the first tail rotor gearbox has completed the fatigue test with a good result, and the first main rotor gearbox has passed 65% of the test programme.

Also the durability tests of the gearboxes under service load are being performed; the first 1800 hours with the casings made from GA8 alloy. Next, the gearbox mechanisms will be transferred to the casings made from AlSiMg0.6 alloy. With these casings, the tests will be carried out up to failure.

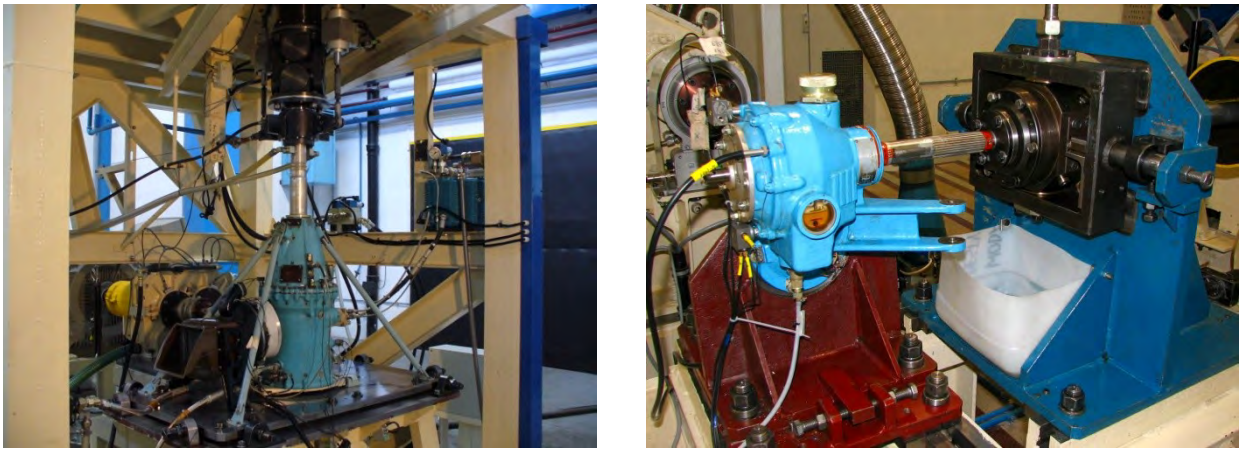

Fig. 1. Durability tests: the main gearbox (left), the tail gearbox (right).

2.2 Helicopter Structural Integrity Program of Polish Army Mi-24 Hind Helicopters

(Andrzej Leski – Air Force Institute of Technology, Warsaw)

In this work selected problems connected with developing Helicopter Structural Integrity Program (HSIP) of Polish Army Mi-24 Hind Helicopters have been investigated.

The problems include:

1. Collecting, analysing and forecasting operational helicopter's failures.
2. Developing FE model of helicopter structure.
3. Operational loads monitoring.
4. Fatigue life estimation.
5. Implementation of modern NDE methods.

In the work the abilities of IT system, the SAMANTA system used in Polish Armed Forces for collecting and analysing operational and maintenance related information have been discussed. Advantages of applying the relational data base technology implemented in the SAMANTA system and based on the Oracle platform have been shown.

In order to develop FEM model of Mi-24 structure reverse engineering (RE) methods have been used. The RE methods made possible helicopter structure to be digitally reconstructed and transferred to FEM software. Two of RE methods have been used:

a) a digital photogrammetry method by means of the TRITOP system,
b) 3D scanning by means of the ATOS III system.

The service loads spectrum was obtained from the operational loads monitoring programme. The stresses and loads at selected points were measured during several test flights.

Moreover, the procedures of helicopter structure fatigue life estimation based on safe S-N curve concept and crack growth concept have been included in the work.

A modified NDE/NDI programme was developed in order to support HSIP. Special attention was paid to detection of subsurface defects such as hidden corrosion and cracks by means of the DSight Aircraft Inspection System (DAIS II), Magneto-Optic Eddy Current Imager (MOI-308) and MAUS V C-scan system.

The above mentioned HSIP was developed by Polish Air Force Institute of Technology under the research project funded by Polish Ministry of Science and Higher Education and Polish Ministry of National Defence.

2.3 Modern automated NDE techniques for composite helicopter main rotor blades inspection

(Krzysztof Dragan – Air Force Institute of Technology, Warsaw)

Composite structures are becoming more popular in the aerospace industry because of their unique features such as: excellent strength/weight ratio, corrosion resistance, possibility of complicate shape manufacturing. An extensive use of composites in Aerospace components nowadays has become real and one of the examples of this trend is Boeing 787 *Dreamliner* aircraft, where nearly 50% of the aircraft structure has been made from composite elements.

The increased usage of composites for aircraft structure influences the necessity of gathering information about structural integrity of such components. The reason for that is the following, during the manufacturing of composites as well as during in-service and maintenance procedures there is a possibility of damage or failure. There is a large number of failure modes which can appear in such structures. These failure modes affect structural integrity and durability. This work presents an approach to detection of composites damage such as: delaminations, disbonds, foreign object inclusion and core damage. This detection is possible with the use of advanced the P-C aided Non Destructive Testing NDT methods. In this work, methods for detection of such damage have been elaborated. Moreover, software based on *Image Processing* and *Mathematica* Library has been developed to evaluate results received from automated systems. This software enables automated determining of damage size based on numerical calculation. In this work, detectability for selected methods and accuracy of elaborated software has been determined.

This work has been performed for the needs of composite main rotor blades of helicopters. These blades are made from Glass Fibre Reinforced elements GFR. In the blades structure, the spar is reinforced with the use Glass Roving material and honeycomb elements are made from Nomex or Glass Epoxy.

This work presents a modern approach to damage detection in the composite main rotor blades of helicopters.

3. AIRPLANE STRUCTURES

3.1 Full-Scale Fatigue Tests of PZL M28 05 SKYTRUCK Aircraft

(Janusz Pietruszka - PZL MIELEC)

The most important tests performed at the Structural Tests Laboratory of Polskie Zaklady Lotnicze in Mielec have been full-scale fatigue tests of the PZL M28 05 SKYTRUCK aircraft (fig. 1).

Fig. 1. PZL M28 05 "SKYTRUCK" aircraft in flight. Twin turboprop, braced wing, fixed landing gear light transport airplane. Unpressurized fuselage. Strut-braced wing. Twin-fin tail.

As this aircraft is certified in commuter category of FAR 23 and CS-23 airworthiness regulations, airframe tests have been performed on two separate rigs:

1) wing and wing carry-through structure fatigue tests (fig. 2);
2) empennage and attached structure fatigue tests (fig. 3).

Fig. 2. Wing and wing loads-carry-through test rig. The test is conducted with MTS Aero 90-LT system.

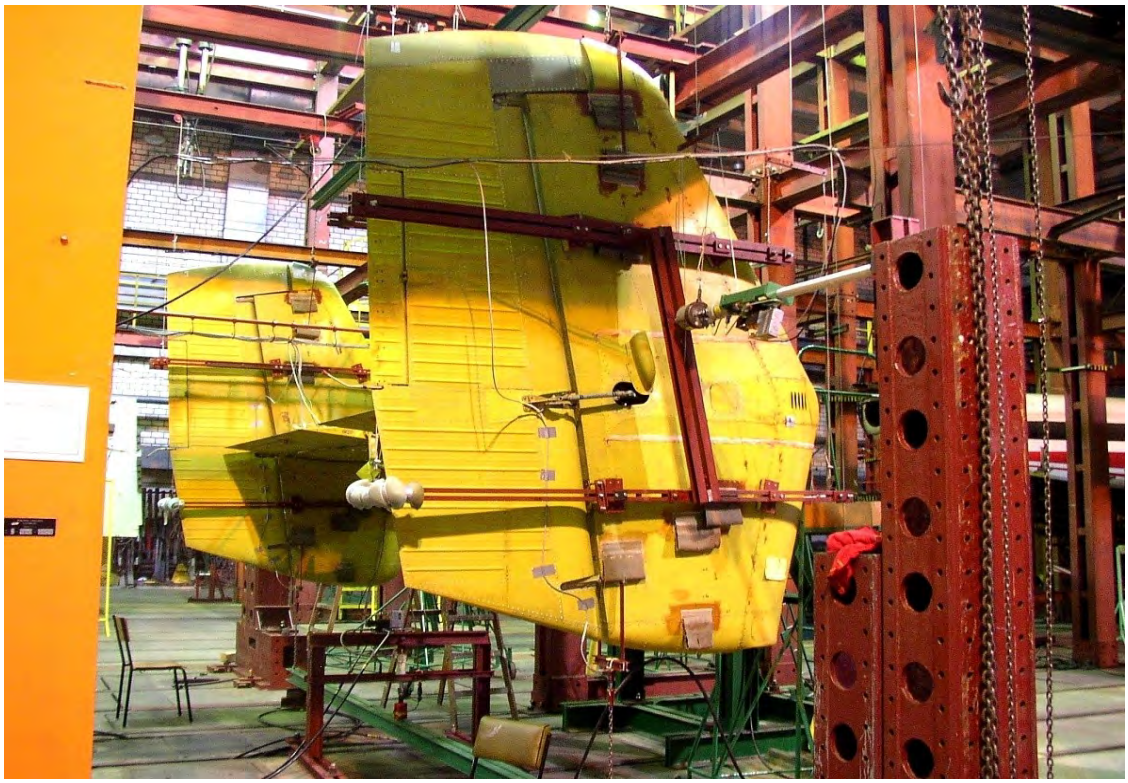

Fig. 3. Empennage test rig in Polskie Zaklady Lotnicze. The test program was prepared by the Institute of Aviation in Warsaw. The loading system was developed at PZL Mielec.

The full-scale fatigue test of the braced wing and the wing carry-through structure was presented during ICAF Conference in Hamburg in 2005. The fatigue tests of the empennage and fatigue tests of the nose landing gear were presented during ICAF Conference in Naples in 2007. Other fatigue tests were also performed: main landing gear fatigue tests and engine mounting fatigue tests.

The goal of these tests was the extension of the service life.

PZL M28 05 airframe design description

The airframe is typical metallic: thin walled, riveted, made from alumunium alloy 2024 or its equivalent D16T. Important fittings and bolts are made from low-alloy high strength steel 30HGSA. Some parts are made from titanium alloy VT-22.

The wing torsion box is limited by front and rear wing spars. Part of torsion box is used as fuel tanks. The wing strut is mounted to the wing with a fitting, which is part of the reinforcement between the wing spars. The wing strut is also mounted to the main landing gear beam. This beam goes through the fuselage central part, as part of the underfloor structure. The wing is mounted to the fuselage with four fittings in the fuselage upper part.

The empennage is H-type, mounted with four fittings to the fuselage upper part. The most loaded element is the stabilizer. Its torsion box is limited by front and rear spars. The stabilizer nose and stabilizer slat are mounted to the front spar by bolts, so may be removed during inspection.

The progress of the tests

Some cracks appeared in the expected areas of the airframe, i.e. in areas of high stress level or high stress concentration according to fatigue analysis. Some cracks occurred in the unexpected areas, i.e. the areas overlooked in the earlier fatigue analysis. These areas were overlooked because of the goal of these analyses, which was to determine the

areas of the shortest fatigue life. As fatigue damage in the expected areas was repaired, the tests were continued and other areas of fatigue damage were discovered. The critical area of the wing structure is the wing strut mounting. The critical area of the empennage is the stabilizer front spar in the area of mounting to the fuselage.

Fatigue damage detection during the tests

Two main methods of crack detection are the visual inspection of tested structure and the strain gauges indications monitoring.

The visual inspection is made in the same way as the maintenance inspection. A very useful idea was implemented in the wing fatigue test, namely fuel in fuel tanks was coloured. It helped to observe cracks in the wing strut mounting area.

The strain gauges measurement during tests is a very popular method of airframe strain analysis validation and fatigue damage detection. On the wing structure more than 100 strain gauges were applied. Some of them were added during the test, in order to better observe the area of interest. On the empennage structure about 20 strain gauges were applied (fig. 4). The analysis of the strain gauges measurements leads to fatigue crack detection (fig. 5).

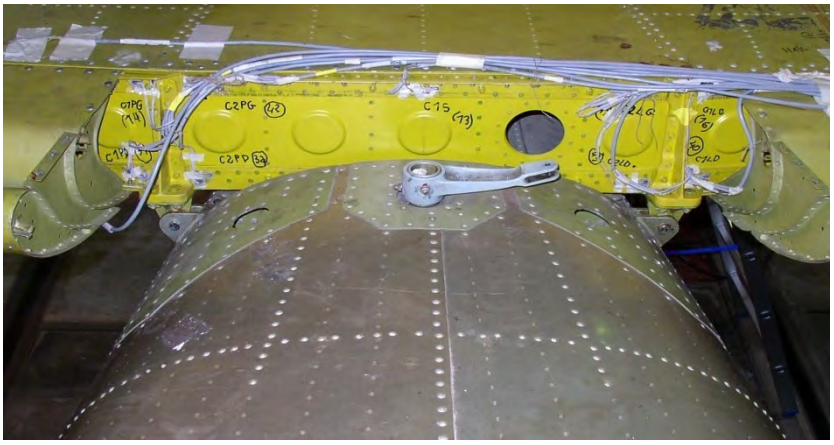

Fig. 4. Strain gauges in empennage critical area. Details of stabilizer front spar and fuselage connection are visible.

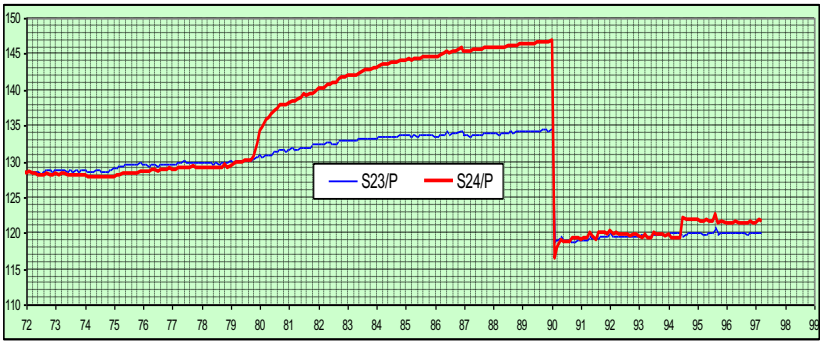

Fig. 5. Strain gauges no S23/P and S24/P maximum indications changes during the test. Indications are scaled in MPa (megapascals). Prior to 80000 simulated flight hours maximum indication of S24/P began to change as a result of the wing skin crack propagation. After 90000 simulated flight hours this area was repaired.

Various methods are used during detailed inspections of damaged elements. These inspections were made by factory's NDT laboratory. The NDT method depends on

damaged part material and other features, e.g. geometry. The magnetic fluid method is the most commonly used.

Safety during the tests

One of tasks in fatigue tests is the prevention of unintentional damage of tested airframe. This may result from an error load applied to the airframe or a loss of rigidity of the tested airframe due to excessive cracks. During the wing fatigue test following means were applied:

- software protection in the control console computer, stopping the test if the load error exceeds the established limit;
- load channel protection in the amplifier in the control console;
- setting a load limit in the loading channel, reducing hydraulic pressure if load exceeds this limit;
- introducing hydraulic actuator stroke limiter, preventing excessive displacement at the loading point (fig. 6);
- reducing hydraulic pressure if the load exceeds the limit;
- setting a limit in the strain gauge channel, stopping the test if the strain gauge indication exceeds the established limit;
- emergency stop button, used by the operator in case of emergency.

Fig. 6. MTS Aero 90-LT hydraulic actuator with stroke limiter, used in order to prevent extensive damage of tested airframe in case of the loss of its rigidity.

Final remarks

The full-scale fatigue tests of the PZL M28 05 SKYTRUCK aircraft were performed at Polskie Zaklady Lotnicze in Mielec for several years. It was a big challenge for structural tests laboratory. Happily, tests were conducted with sufficient care and their results constitute very good basis for the extension of the aircraft service life.

3.2 The Fatigue Life Assessment of PZL-130 ORLIK Structure Based on Historical Usage Data

(Andrzej Leski – Air Force Institute of Technology, Warsaw)

The PZL-130 Orlik has been designed and is operated according to the 'safe-life' approach. The aircraft's flying time is the parameter that controls operation of each aircraft. All the Orlik airplanes operated by the Polish Air Force are equipped with digital flight recorder S3-1. Flight recorders deliver data for the whole population of the Orlik aircraft operated by the Polish Air Force and are available for fatigue-wear assessment of aircraft structures.

Owing to the efforts of the Air Force Institute of Technology in Warsaw, the Orlik operational data that cover the total time of operating these airplanes by the Air Force of Poland have been captured. The collected database includes over 36,000 files, each representing a single flight. Unfortunately, all the data are in the compressed form, hence, all the signals are available at the sampling frequency of 1 Hz. The sampling frequency of 1 Hz is sufficient to reconstruct loads that affect the aircraft structure except ground manoeuvres and the moment of landing.

The aim of this work was to find the way of fatigue wear estimation for PZL-130 ORLIK aircraft based on the historical data from flight recorders.

Since the recorders on the Orlik aircraft do not record the weigh-on-wheels signal, the take off and landing moments are hard to find based on n_z signal only (fig. 1). Some other recorded signals were used to find the take-off and landing moments. Algorithms for this were developed. The following inputs are used in these algorithms:

- pressure height,
- airspeed,
- engine torque,
- oil pressure,
- lowering the undercarriage.

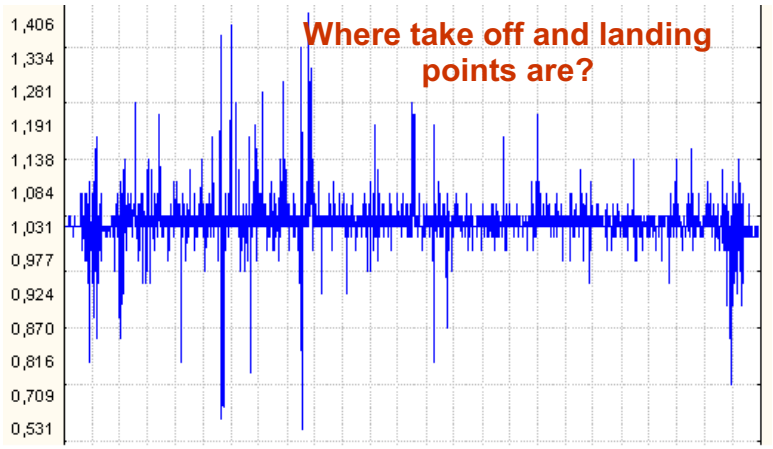

Fig. 1. The n_z signal for one flight

The rest of the data representing all other flight phases were processed with a cycle-counting algorithm. Different algorithms were used. The one used in this study was the rain-flow counting method.

Fatigue calculations were made with the S-N curve method. The safe S-N curve is based on the mean S-N curve after some extra safety rates have been introduced in the equation that describes it. The most essential objective of applying the safe S-N curve is

to take into account the statistical scatter in fatigue life. The mean S-N curve was the basis to find the safe S-N curve for the material 2024T3, the notch factor $k_t = 2$, and the mean value $\sigma_m = 0$.

The numerical relationship for the mean S-N curve is described with the following dependence:

$$\log \overline{N} = 12 - 3.33 \log\left(S_{eq} - 84.83\right) \tag{1}$$

or

$$S_{eq} = 10^{\frac{12 - \log \overline{N}}{3.33}} + 84.83 \tag{2}$$

where:

$\overline{N}$ – life (number of cycles)

S_{eq} – equivalent amplitude of the cycle determined with the following formula:

$$S_{eq} = \sigma_{\max}\left(1 - \frac{\sigma_{\min}}{\sigma_{\max}}\right)^{0.68} \tag{3}$$

where:

σ_{min} – minimum stress in the cycle (in MPa),

σ_{max} – maximum stress in the cycle (in MPa).

The safe S-N curve was accepted for the calculations, one that was originated by means of displacement downwards by the value of 45 MPa because of the statistical scatter in results of fatigue tests. Furthermore, an additional factor, which increased the equivalent-cycle amplitude by 30% was introduced.

The analytical form of the safe S-N curve is expressed with the following formulae:

$$\log \overline{N} = 11.62 - 3.33 \log\left(S_{eq} - 30.6\right) \tag{4}$$

or

$$S_{eq} = 10^{\frac{11.62 - \log \overline{N}}{3.33}} + 30.6 \tag{5}$$

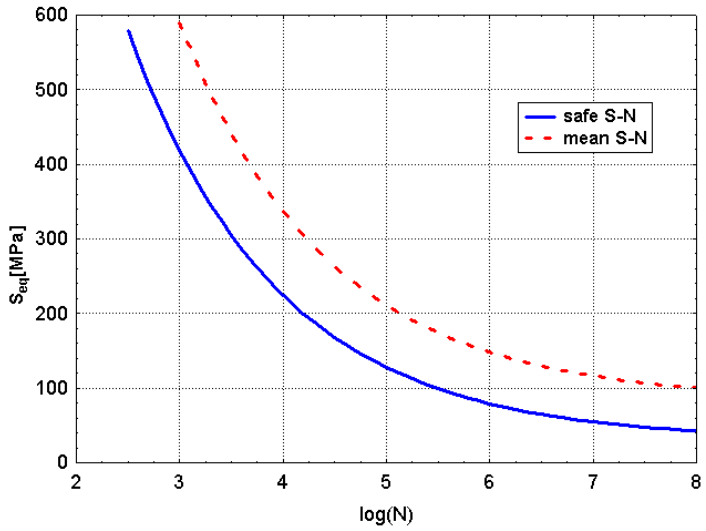

Fig. 2. The mean and safe S-N curves for the material 2024T3

The level of stress to which the structure is exposed proves of essential significance to the structure's life. The stressed skin that constitutes the lower surface of the wing box has been recognized as critical area in the Orlik's structure because of its susceptibility

to fatigue failures. Correlation between the stress and the g-load affecting the Orlik can be estimated based on:

- strain gauge measurements, and
- numerical calculations.

In the year 2000, the Air Force Institute of Technology took part in the measurements of loads for the Orlik aircraft. One of the strain gauges was placed in the localization critical from the fatigue point of view, i.e. on the lower part of the wing spar.

The recorded parameters are presented in fig. 3.

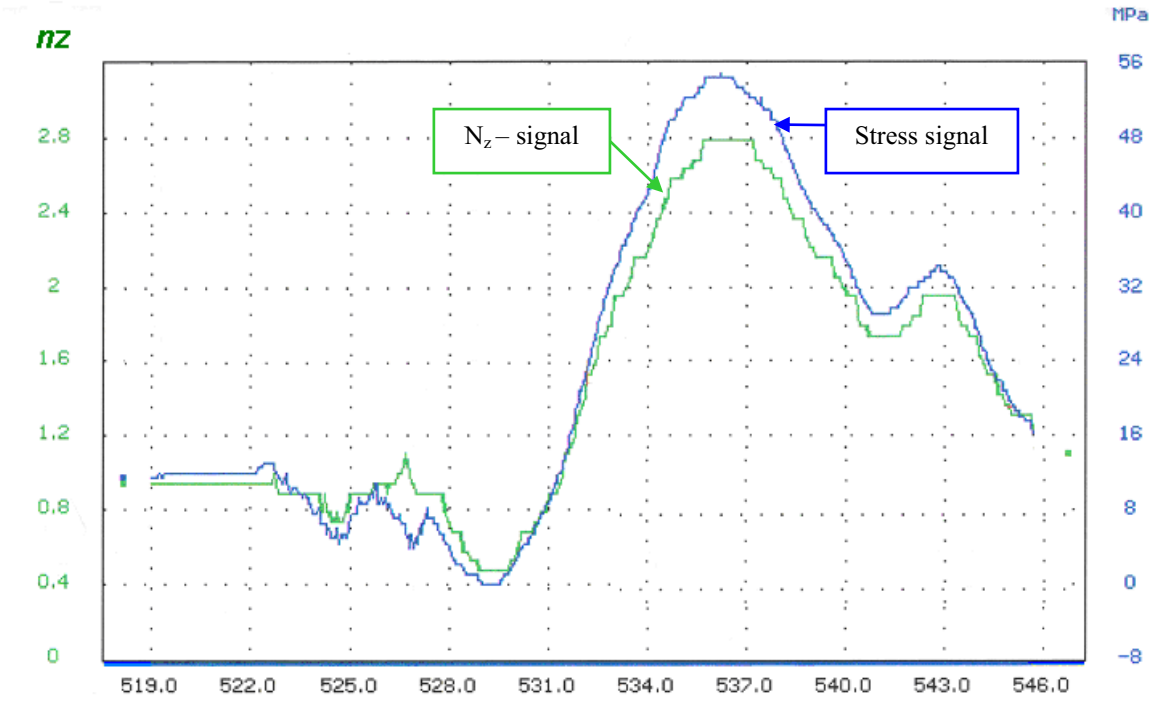

Fig. 3. Changes in the courses of signals – an original drawing

Based on fig. 3, the correlation between the g-load and the stress can be written down with the following formula:

$$\Delta\sigma_k = 22.5MPa \cdot (\Delta n_z) \tag{6}$$

where:

$\Delta\sigma_k$ - change in stress in the critical localization.

The FEM model of the Orlik has been built in the EADS PZL "Warszawa-Okęcie" S.A. using the MSC Patran/Nastran software. It is a global model that allows the indication of critical areas on the Orlik's airframe structure, and of stress values in the indicated areas. To find local values of loads, these areas should be considered in more detail, which means local models should be introduced.

Fig. 4 presents a FEM model consisting of approximately 3.5 thousand tri and quad surface elements that make up the skin of the wing modelled, and approx. 4.5 thousand two-node bar elements that compose the primary structure. Because of the way of feeding loads into the model, no consideration has been given to mass components such as the undercarriage, assemblies, fuel tanks, etc.

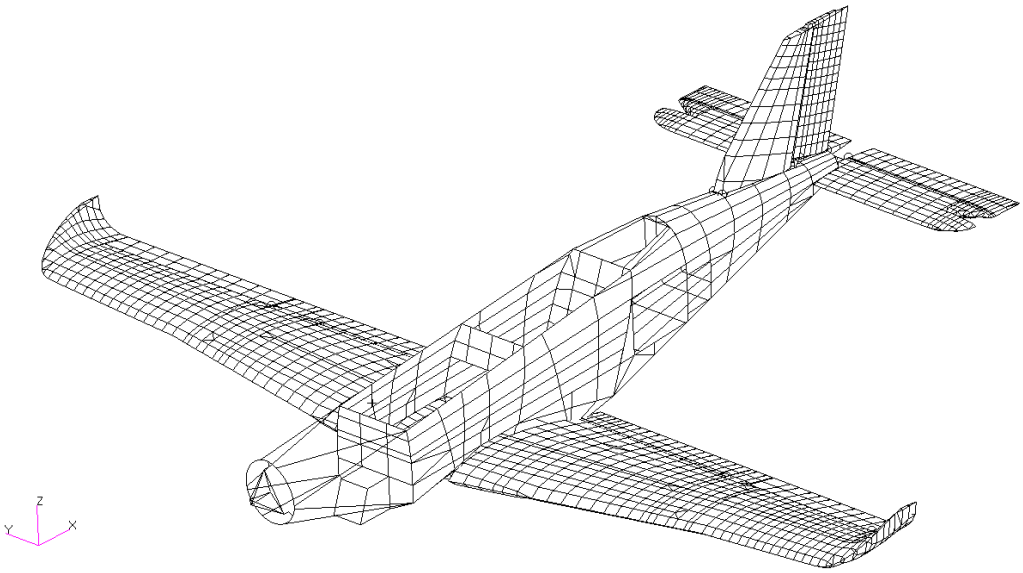

Fig. 4. The FEM model of the PZL-130 Orlik

The results of numerical calculations gained after the FE model had been loaded with the pressure distribution suitable for point A of the manoeuvring envelope n_z= 6 g, V = 400 [km/h], and Q = 2400 kg, have been presented in fig. 5.

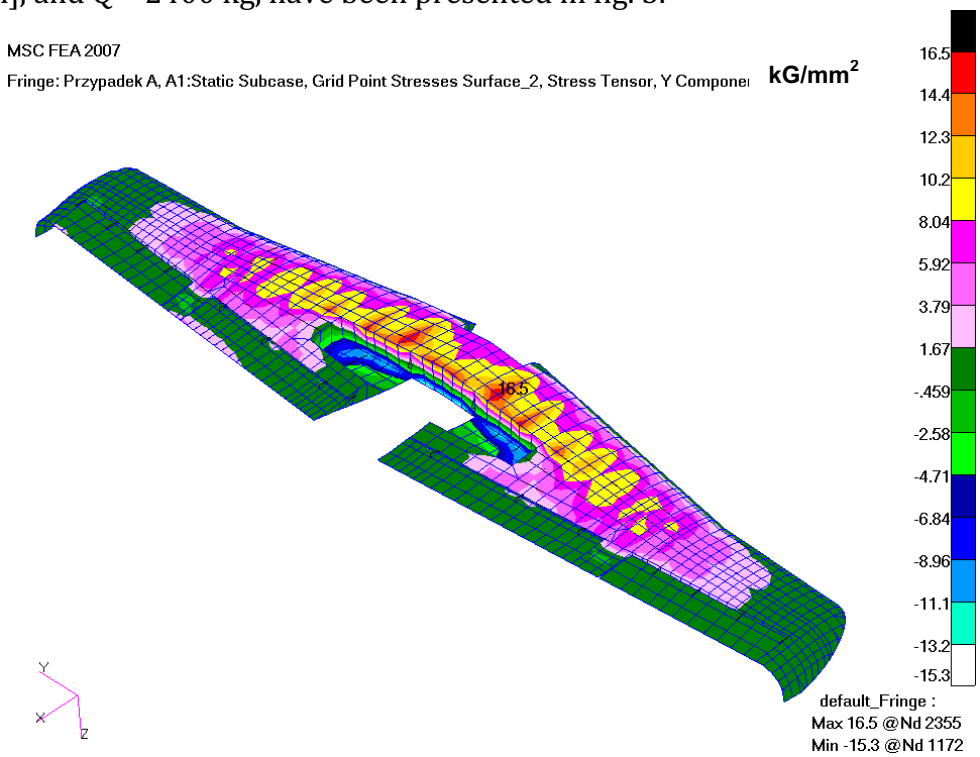

Fig. 5. Stress distribution for the lower wing skin

With the FEM calculations applied, the relationship between the stress and the g-load has the following form:

$$\Delta\sigma_k = 27\,MPa \cdot (\Delta n_z) \tag{7}$$

The fatigue calculations methodology distinguishes the manoeuvres-induced fatigue of the structure from that generated by gusts. In spite of a different nature of each of these effects, their impact upon the structure remains very similar –both produce

fatigue of materials. No flight data recorder distinguishes manoeuvres-induced loads from those effected by gusts. Calculations of fatigue failures were made for each of the aircraft loading spectra (normalized to the amount of 1000 flight hours). The safe S-N curve was applied to do calculations.

A fatigue failure that occurred during the flight was found following the Palmgren-Miner linear cumulative damage hypothesis.

$$D_L = \sum_i \frac{N_i}{\overline{N}_i} \tag{8}$$

where:

D_L – in-flight fatigue failure,

N_i – the number of cycles for individual aircraft for total flight time normalised to the amount of 1000 hrs,

$\overline{N}_i$ - the number of fatigue cycles to failure at some specific loading level, where

i - the number of amplitude levels and mean values used while counting the cycles.

It has been presumed that the GAG cycles put some changes in stress in the critical airframe localization (the lower wing skin) somewhere between the maximum stress recorded during a flight (σ_{GMAX}) and the minimum stress that occurs while on the ground or in the course of flight (σ_{GMIN}). The change in the mean stress level for the 'on-ground' and 'in-flight' positions of the aircraft results from the change in the configuration of loads that affect the aircraft structure.

In Figure 6 a part of data recorded during flight tests and illustrating the very moment of landing has been presented. The blue line corresponds to the change in stress in the lower wing skin. This localization is very close to the area for which fatigue analysis is carried out. The figure 6 shows changes in stress during the landing that allow us to conclude that the change in load configuration during the landing results in the reduction of mean stress by approximately 12.5 MPa.

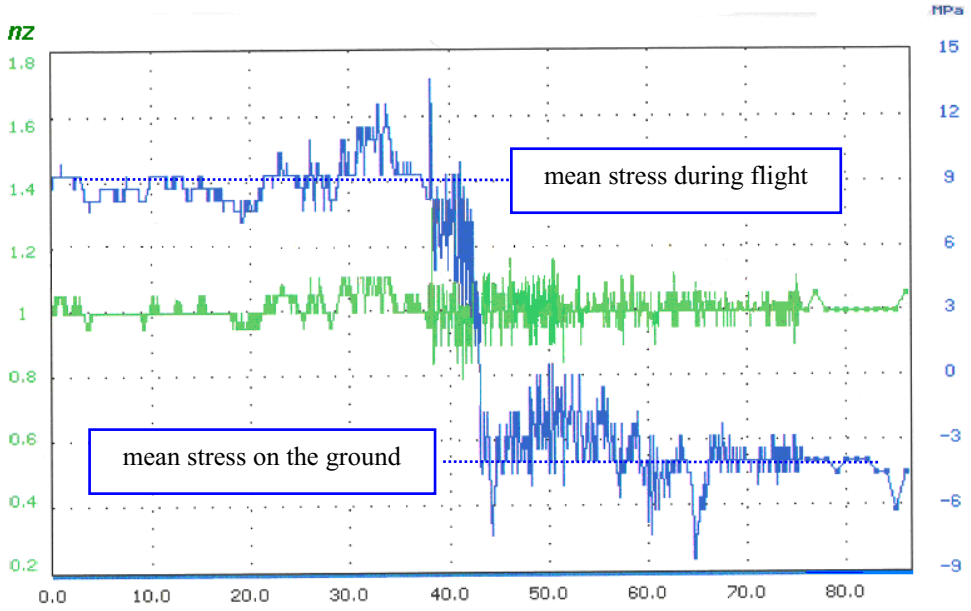

Fig. 6. The courses of signals during the landing

Total fatigue damage of the airframe is found as a sum of failures during the flight, on-ground manoeuvres, the landing, and those induced by GAG cycles. Summation requires

that account is taken of aircraft's flight hours and data capture rate ψ. Furthermore, the landing and GAG cycles induced failures depend on the number of landings performed by the aircraft. The total fatigue failure can be found from the following formula:

$$D = \frac{T}{1000}\frac{1}{\psi}D_L + \frac{1}{\psi}\left(D_{LG} + D_{LD} + D_{GAG}\right) \tag{9}$$

where:

D_L – damage to aircraft structure during the flight,
D_{GAG} – GAG cycles induced damages,
D_{LG} – damages effected by manoeuvres on the ground,
D_{LD} – the landing attributable fatigue failure,
T – aircraft's total flight time [hours], found from the aircraft documentation,
ψ - data capture rate.

Fatigue failures effected by manoeuvres on the ground

With the courses of n_z recorded during actual flights one can find that values of recorded cycles and frequencies thereof suggest that fatigue failures effected by manoeuvres on the ground should be ignored during the Orlik operation/maintenance.

$$D_{LG} = 0 \tag{10}$$

The landing attributable fatigue failure

The landing attributable fatigue failure is difficult to estimate using the recorded parameters. The signal sampling frequency in the flight data recorder is too low to reliably describe the nature of the landing by means of changes in n_z. Also, finding the vertical speed during the landing (by means of differentiating the pressure height signal) does not give reliable results. The following formula has been accepted:

$$D_{LD} = N_L \cdot 6.04 \cdot 10^{-6} \tag{11}$$

where:

D_{LD} – the landings induced fatigue failure,
N_L – the number of aircraft landings.

The calculations made on the basis of the algorithm presented above allowed fatigue damage determining of the whole population of in-service airplanes. The data from years 1996÷2007 have been used for the calculations. Figure 7 presents fatigue damage for the chosen group of 15 airplanes. Simultaneously, the same figure presents the flying time of these planes. The intensity of particular plane usage can be estimated from the comparison of fatigue wear and flying time.

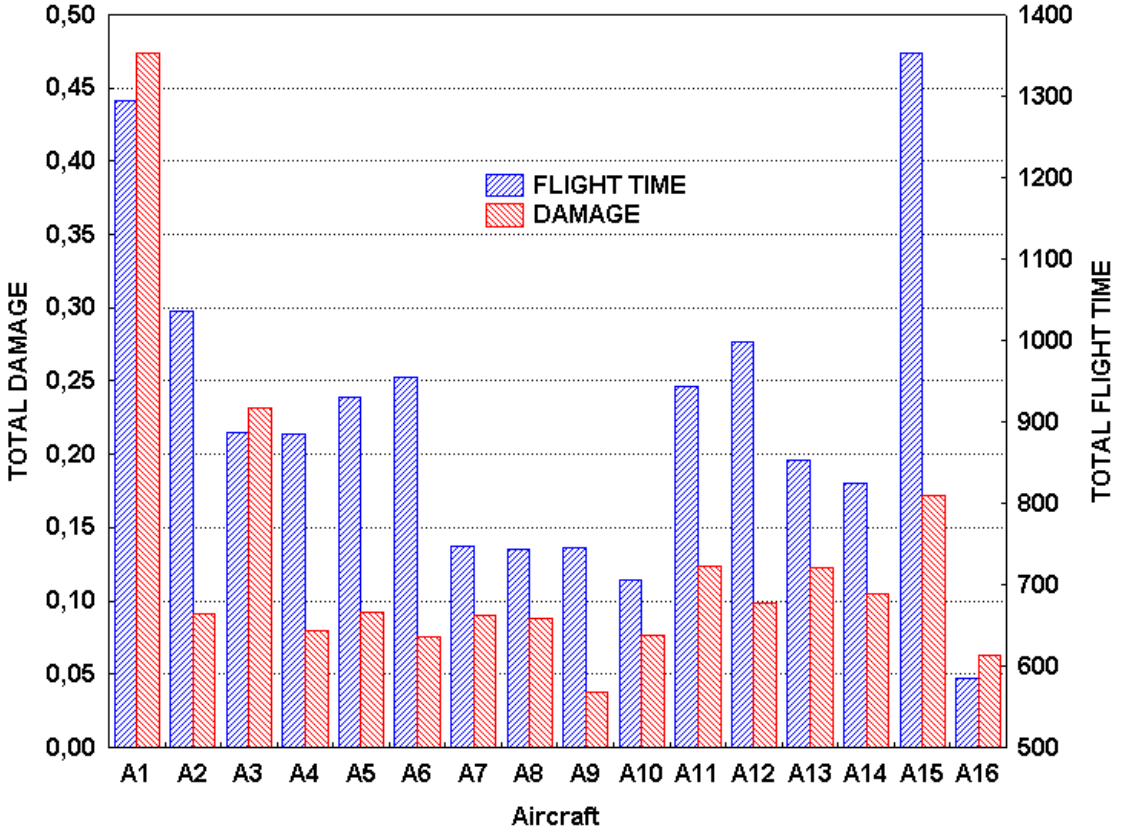

Fig. 7. Results of calculations of fatigue wear

Based on the conducted analysis the following conclusions can be formulated:

a) There are significant differences in intensity of usage, flying time and fatigue wear among PZL-130 Orlik airplanes.
b) Based on service life determined by flying time, the use of Orlik airplanes is not optimal from structural durability point of view.
c) Fatigue damage from maneuvers in the air have the greatest share in structure fatigue of Orlik aircraft.
d) Increasing the frequency of recording and processing nz signal will allow taking into account the influence of gust on fatigue wear.

3.3 Static and Fatigue Tests of the A400M Subcomponents

(Sebastian Szałkowski – Institute of Aviation, Warsaw)

Static and fatigue structural tests of the A400M aircraft subcomponents were carried out at the Institute of Aviation in Warsaw to the order of EADS CASA in Madrid.

The Institute of Aviation designed and built the test set-up and installed the hydraulic loading system, the control system (MTS Aero 90) and the measurement and the data acquisition system for all tests.

During the years 2006 - 2008 tests of the A400M engine cowl subcomponents (doors) were carried out. Specimens consisted of titanium hinge fitting or latch housing joined to representative carbon fiber reinforced plastic (CFRP) panels of the surrounding area. Static test specimens included artificial defects and damage on the CFRP panels. Together 5 static tests and 1 fatigue test were carried out.

Figure 1 shows the test set-up with hinge fitting specimen (one of the configurations) and figure 2 shows the test set-up with latch housing specimen. Tens of channels for the strain gauges and 3 displacement transducers for each specimen were required to measure behavior of the specimen structures during the static and fatigue tests.

Fig. 1. Test set-up with the A400M engine cowl door hinge fitting specimen.

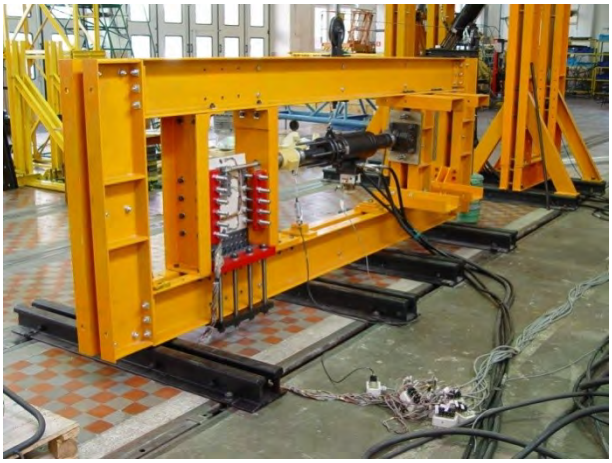

Fig. 2. Test set-up with the A400M engine cowl door latch housing specimen.

The static tests were performed up to the limit load and then to the ultimate load and failure of the specimens. Specimens were inspected visually and with NDT (high frequency eddy current method for metallic parts and ultrasonic method for CFRP panels). All 5 specimens successfully withstood required limit and ultimate loads.

The fatigue test was concerned with the metallic parts of the specimen and consisted of three phases: fatigue, damage tolerance and residual strength test. The inspection program included visual inspections and non-destructive inspections (high frequency eddy current method for metallic parts). The specimen successfully withstood limit loads during residual strength test after damage tolerance phase. Both static and fatigue tests were carried out at room temperature.

At present, certification tests of actuator hinge fitting of A400M vertical tail plane (VTP) is carried out at the Institute of Aviation. One specimen is tested both under static and fatigue loads. Specimen consists of the hinge fitting and representative part of the VTP carbon fiber composite box. Figure 3 shows the test set-up with the specimen.

Fig. 3. Test set-up with the A400M VTP actuator hinge fitting specimen.

3.4 In-service Flaw Detection and Quantification in the Composites Structures of Aircraft

(Krzysztof Dragan – Air Force Institute of Technology, Warsaw)

Composite structures are becoming more popular in the aerospace industry. The greatest advantage of composite materials is strength and stiffness combined with lightness. Composites, by choosing an appropriate combination of reinforcement and matrix material, can show properties that exactly fit the requirements for a particular structure for a given load distribution. A composite airframe is usually more integral than a metal one.

Typically, a single non-destructive method used for inspection of metal structures is not efficient for different types of damage and different composites. The most popular method for NDT of composites is UT with a C-scan presentation mode. This method is very good for fast and easy data collection and inspection results assessment.

Techniques and Types of Damage

Non destructive testing of MiG-29 vertical stabilizer was focused on CFRP (Carbon Fiber Reinforced Plastic) skin. Damage was classified as:

- Delaminations- separation between layers of composite;
- Disbonds- lack of adhesive;
- Porosity- poor resin area;
- Foreign object inclusions- inclusion of non - inherent materials.

Techniques used for inspection of MiG-29 vertical stabilizer and F-16 horizontal stabilizer are as follows:

Technique/Damage	Resonance	Shearography	UT
Delamination	-	-	-
Disbond	+	+ (core-skin disbond)	+
Porosity	-	-	+
Foreign Object Include	-	-	+

Ultrasound Inspection with the Use of Maus® System

Pic. 1. Composite vertical stabilizer inspection.

To perform structural integrity test of the airplane composite vertical stabilizer, ultrasound testing was carried out. The total surface area for inspection was approximately 11 sq. meters per one aircraft. The aircraft population selected for tests was more than 30. So, the total area for inspection was more than 360 sq. m. Classical tests with use of manual hand scanning were very difficult or impossible because work was done on the airplane. The automated scanning procedure was applied. The MAUS ®V system was used. The MAUS® system (Mobile Automated System) is an hybrid construction and makes possible inspection with such techniques as: ultrasound, eddy current, MIA, Pitch-Catch, Resonance and with the Phased Array module for ultrasound. The system is fully portable and enables inspection on horizontal and vertical inverted surfaces. This is possible due to a flexible track system equipped with a special handle. In picture 1 inspection of the vertical stabilizer composite skin of MiG-29 is presented.

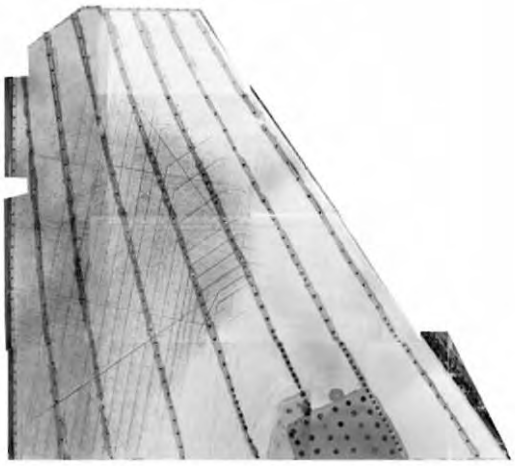

Pic.2. Amplitude C-scan F-16 horizontal stabilizer

Resonance & UT inspection with MAUS system are quantitative methods. Results are presented in the C-scans mode. The MAUS® measurement interface gives possibility of Amplitude and TOF (Time Of Flight) C-Scan data presentation. In pictures 2 and 3 C-scans (Amplitude C-scan of F-16 horizontal stabilizer and TOF C-scan of MiG - 29 vertical stabilizer) are presented. For the amplitude data different colors correspond to different signal attenuation. The amplitude mode is useful for detection of disbonds. The color range in the TOF data gives information about different composite skin thickness values as well as about delamination depth. This system of data presentation is very helpful for damage description as well as for fast damage location finding. If we need more information about damage we can do additional full waveform capturing with B-scan visualization. This method is applied for detection of delamination and foreign object inclusion.

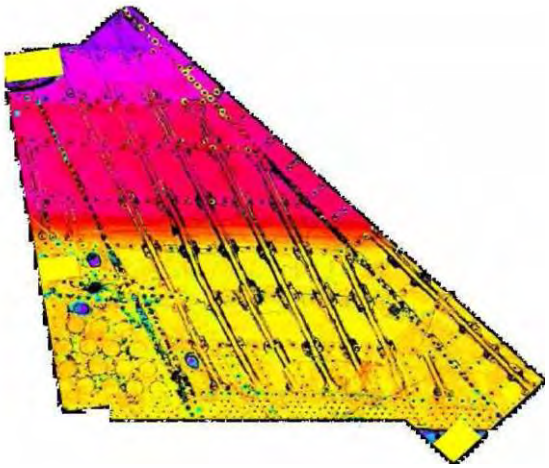

Pic.3. TOF C-scan MiG-29 vertical stabilizer

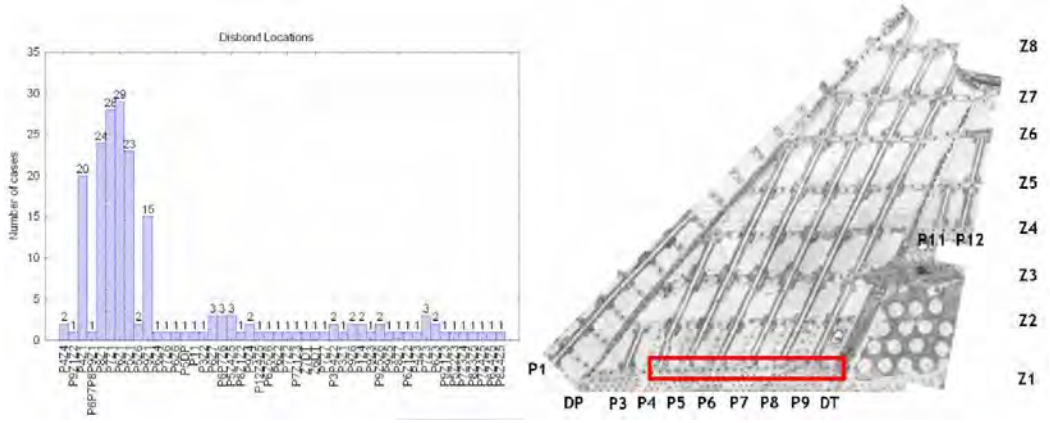

Pic.4. Distribution of damage in MiG-29 vertical stabilizer

Inspection of Sandwich Structures

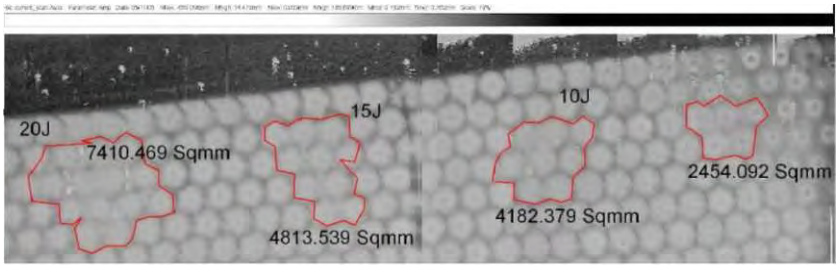

Pic. 5. MIA results main rotor blade inspection

A very effective technique for damage detection in sandwich structures is the Mechanical Impedance Analysis. Another method is the Laser Shearography. This method is very fast and sensitive (specially for thin skin sandwiches) but result is only qualitative (yes/ no). MIA gives an answer of the question: is it a damage?

It also gives information about the size of damage. Some NDT methods are applied to honeycomb sandwich structures (like a W3 composite main rotor blade inspection Pic.5).Very interesting results were obtained during the inspection of B1-PW-5 glider wing. The skin of this wing is a sandwich with a 5 mm DIVINYCELL foam core. For the reason of high attenuation of ultrasonic signal in the foam core an inspection of this kind of structure is very difficult. A low frequency signal that we use in MIA methods is much better for the foam core inspection. A C-scan image gives one-valued information about the condition of bond line between the spar and sandwich skin. The inspection test probe (Pic.6) consists of sandwich panel and laminated spar gives us the same result. The additional test probe consists of two small disbonds (1sqmm and 1.5 sqmm) which are visible in the C-scan (Pic.7).

Pic. 6 Test specimen

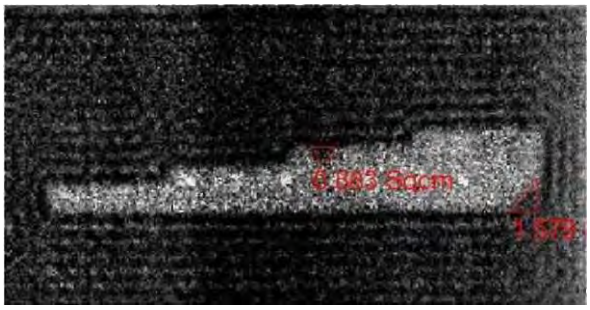

Pic. 7 MIA test results

Structural Health Monitoring

Applying NDT to composites is necessary from the point of view of their applications not only in the rotorcraft industry but also in the other aircraft structures. A continuous development of extensive use of composites in the aerospace applications puts great demand on the advanced techniques of NDT as well as on the health monitoring techniques. One of the big advantages of the use of advanced NDT techniques is the possibility to obtain the information about structural integrity of composites without affecting structure properties and to collect data for structure monitoring. One of the disadvantages is the necessity to have the aircraft on the ground, which involves human staff and time for inspecting all locations. Applying network sensors distributed in the

structure for periodical or even continuous monitoring could affect the time necessary for the inspection. The so called Structural Health Monitoring SHM gives a possibility to deploy NDT with greater access to more complex structures. According to D. Roach, "The core of SHM is development of self-sufficient systems, which use built-in distributed sensors/actuators not only to detect structural failures but to monitor the effects of structural usage".

Using sensors networks could be realized in three approaches which are listed below:

- In-situ sensors;
- Sensors network with in-situ data acquisition;
- Sensors network with real-time data transmission to a remote site.

In the first group sensors are permanently installed in the structure. For the diagnostic purposes an aircraft must be on the ground. All necessary items such as power supply, data acquisition electronics must be delivered to the aircraft. All sensors are connected to the connector and data analysis and detection procedures are performed on-site. From that point of view, manual or automated collecting data are substituted by distributed networks. In the second group, distributed networks are equipped with the electronics and memory to record and to store data. *„Those items are equipped with programmable circuits having the power for automated data logging in flight or on the ground"*. Data must be gathered by the technical staff during the aircraft stay on the ground.

The third group is quite similar to the second group. The only difference is the usage of the communication system application. That system enables wireless transmission of collected data. For that particular application software could be developed to send data to the maintenance personnel.

There is a lot of work which is dedicated to possibility of applying SHM especially to aircraft as well as to composites. The use of in-situ sensors for the SHM of aircrafts seems to be viable option in the near future.

The Air Force Institute of Technology is R&D center supplying solutions for Polish Army mainly connected with aging aircraft program. That role was presented on the base of introducing new maintenance approach for the MiG-29 and F-16 aircraft.

3.5 Investigations into Glider Landing Gear Load Spectrum

(Wojciech Owczarek, Mirosław Rodzewicz – Warsaw University of Technology, Warsaw)

Goal of the research

The research goal was to study the load spectrum applied to a glider main and front landing gear during takeoffs and landings on different kinds of airfield surfaces, and comparison of different methods used to analyze the obtained load records.

The research contained a description of the tests carried out on a PW-6 glider.

Data analysis included a comparison of different methods of post processing the load records. To analyze the data a set of software was developed that allowed processing the records using a particular method.

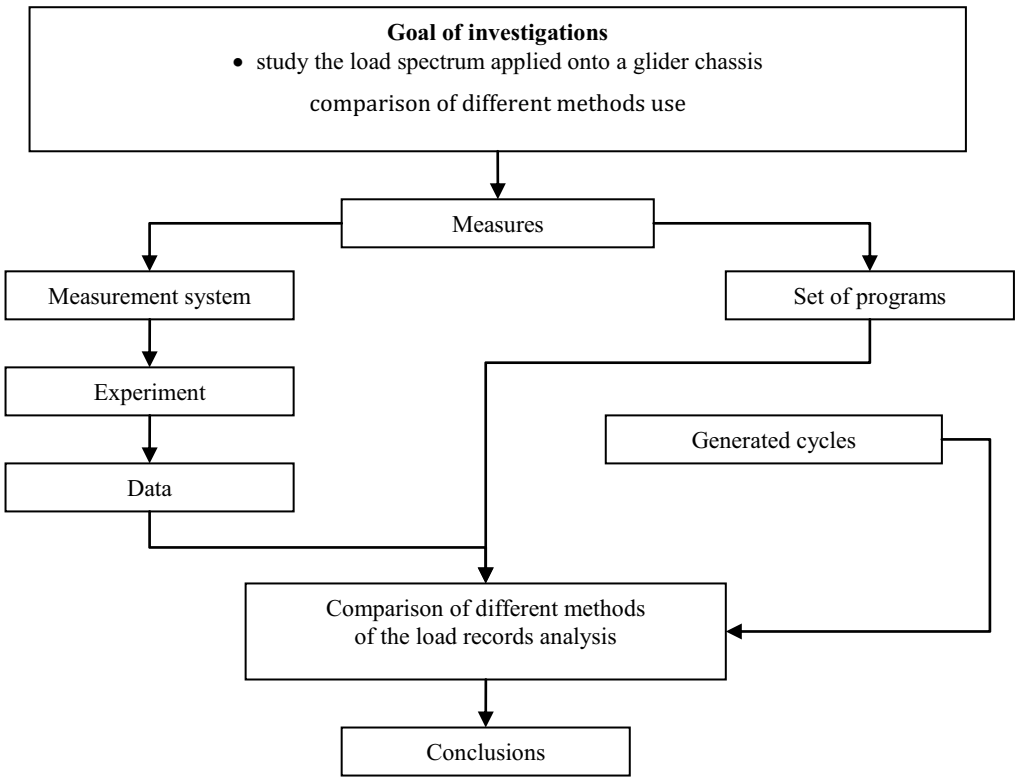

Fig. 1. Operational scheme

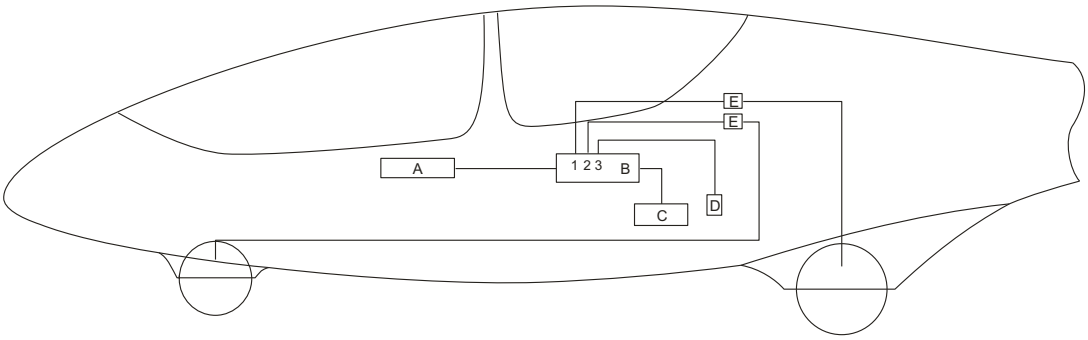

A - recorder
B - distributor
C - battery
D - accelerometer
E - signal amplifier

Fig. 2. Whole measurement installation scheme

Set of software

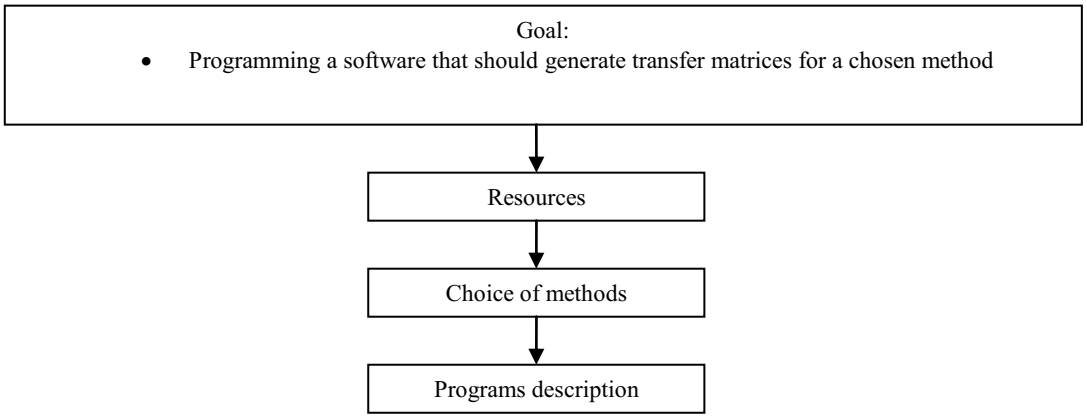

Fig. 3. Operational scheme

Choice of methods

To make the comparison of particular methods of Full Cycle Counting (FCC) possible a number of programs were written. The following outputs were compared:

- Transfer matrix
- envelope method (based on rain flow counting)
- local extremes counting method
- level exceeds counting method
- progressive filtering counting method
- quasi rain flow counting method.

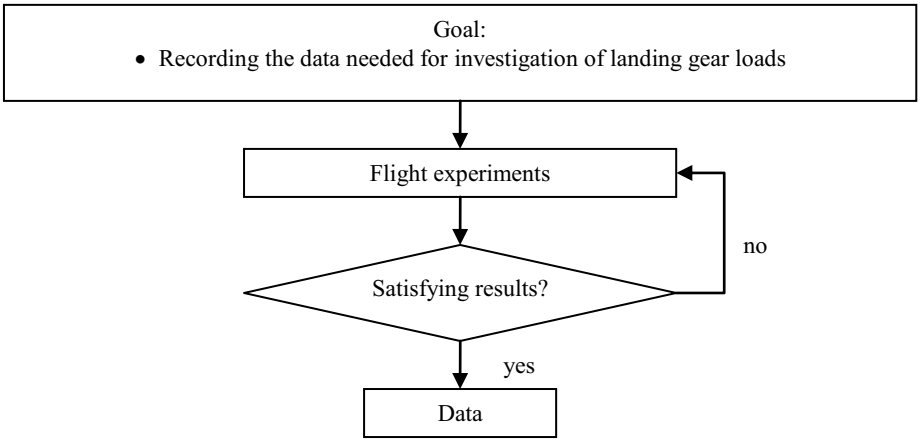

Fig. 4. Operational scheme

Flight experiments

Flight experiments were taken on a grassy air field. The data was collected during six landings and takeoffs of the glider. Sampling frequency applied during the recordings was 100 Hz.

Data

An example of recorded signals is shown below. The graphs show the voltage values (in mV) of signals of main gear load, front gear load, acceleration and velocity (based on pressure measurements).

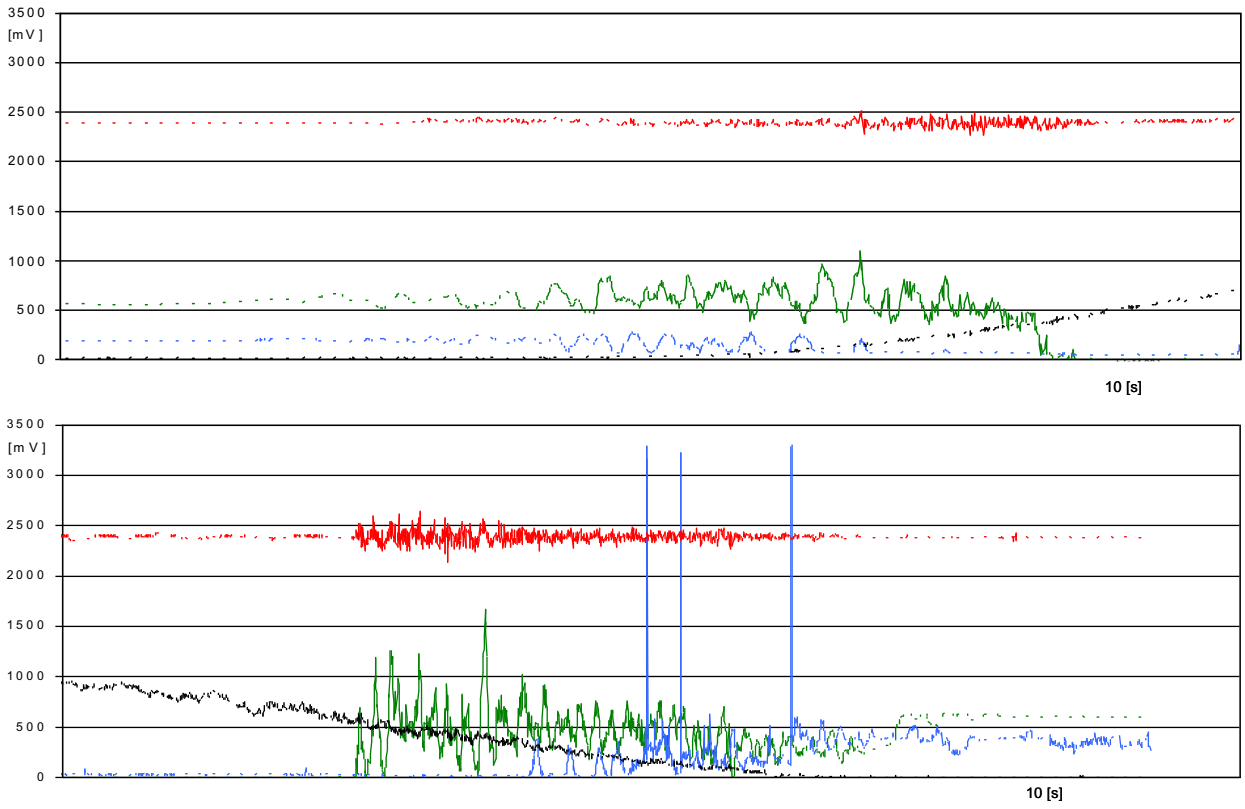

Fig. 5. Sample of registered signals

Comparison of methods used to process the load records

Analysis

Based on the records transfer matrices were generated. Next, a cumulated damage D value was calculated according to Palmgren-Miner hypothesis. Fig. 6 shows the ratio of D (separate for each investigated method) to the value of D taken from the transfer matrix (treated as the reference) in function of I coefficient (where I is the ratio of the number of local extremes over the number of mean value exceeds in time)

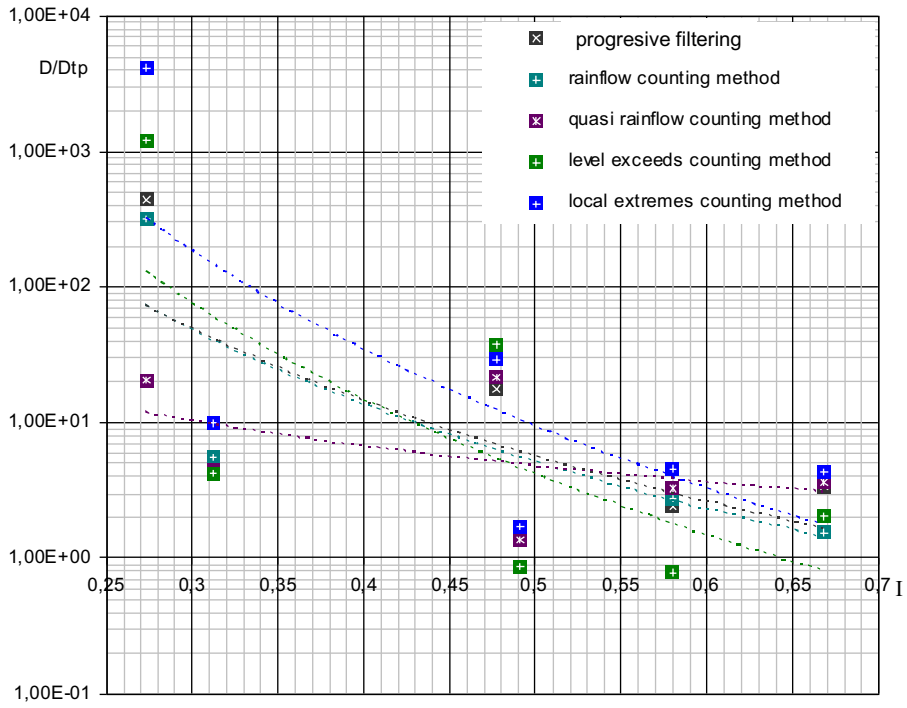

Fig. 6. Comparison of FCC methods

Conclusions

Load spectrum

The goal of the research was to investigate the load spectrum of a glider landing gear. On the basis of local extremes count method (it gives the biggest values of D coefficient) a block-spectrum of loads was generated (Fig. 7, 8), which is the answer to the stated problem. The graphs show the mean value of cycles from all the flight experiments. On the horizontal axis: number of cycles, on vertical axis: relative load F/Q where: F - current load exerted on the gear, Q – load exerted on the glider gear when the glider is standing on the airfield, ready to fly.

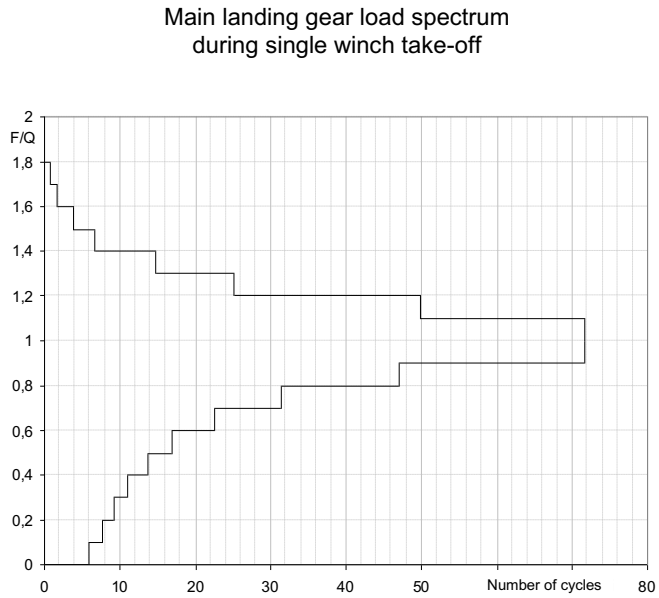

Fig. 7. Load spectrum of the main gear during a single takeoff with a winch.

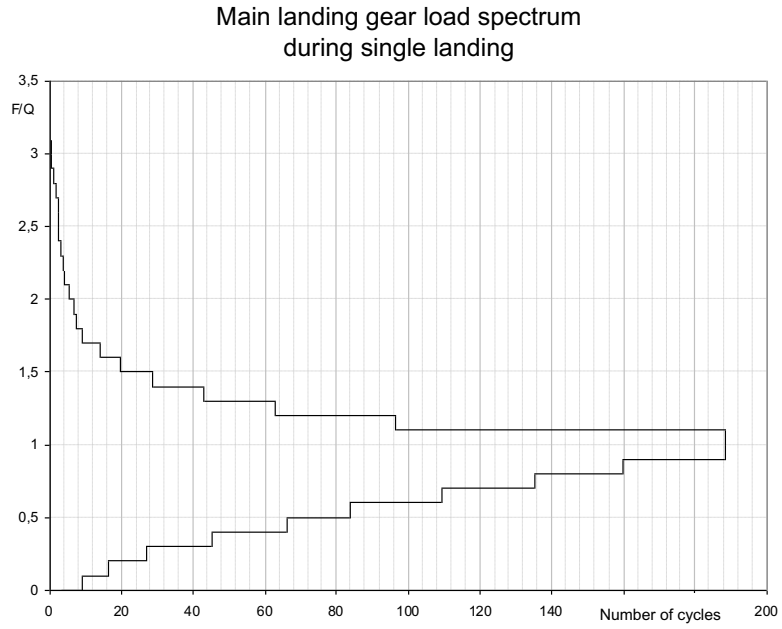

Fig. 8. Load spectrum of the main gear during a single landing on a grassy airfield.

Comparison of methods processing random series of load spectrums

For each FCC method an increase of coefficient D was observed in comparison to the value calculated from transfer matrix. The differences reach a few orders and are the biggest for irregular cycles with small values of I coefficient. Coefficient I is in the range of 0,5-0,9 for the cycles observed in the nature. For those values of I the difference of D between the methods investigated decreases but the estimated fatigue life (which is proportional to 1/D) is still different by several times for each FCC method.

Local extremes count method – gives the highest value of D coefficient, but because it ignores the sequence of loads it might be expected to be less precise than e.q. rainflow counting method. Besides, it requires the mean value of loads.

Level exceeds count method – in two cases the value of D was even smaller than the one from transfer matrix.

The rainflow counting method – is considered as the best FCC method. As the only one respects the cycles sequences, which makes it the most complicated one. Additionally, it requires the whole signal time course to be kept in the memory while processing.

The progressive filtering counting method – gives the results comparable to the rainflow counting method and shares its basic disadvantages – complicated computing, possible only when based on a load level series. The resulting transfer matrix is diagonally symmetrical, which is useful while organizing fatigue tests.

The quasi rainflow counting method – in comparison with other methods, it lowers the results for small values of I coefficient.

4. MATERIALS TESTING

4.1 Strength Testing and Analysis of Fatigue Crack Growth in Selected Aircraft Materials

(Sylwester Kłysz – Air Force Institute of Technology, Warsaw)

The study has been intended to determine the most essential mechanical and fatigue properties as well as impact strength of the 30HGSNA steel, to gain own data on the above-mentioned characteristics of materials to be used further on in numerical analyses of life estimates of aeronautical structural components. The scope of the study comprised the following assignments:

1. determination of the most fundamental mechanical properties and impact strength of materials,
2. low-cycle fatigue testing and evaluation of the Manson-Coffin curves,
3. high-cycle fatigue testing and evaluation of the Wöhler curves,
4. investigation into fatigue crack growth rates at constant and variable load-cycle amplitudes (determination of curves $da/dN = f(\Delta K, R)$, coefficients in Paris and NASGRO equations, coefficients in the Wheeler models of delay, the value of $K_{th}(R)$),
5. crack toughness testing under the plane-state-of-strain conditions at room temperature (determination of the $K_{Ic}(R)$).

The strength/fatigue testing was carried out in the Laboratory for Materials Strength Testing of the AFIT's Division for Aeronautical Systems Reliability and Safety, the lab being accredited by the Polish Centre for Accreditation (Accreditation Certificate No.: AB 430).

Preparing for the testing work

The 30HGSNA is a constructional alloy steel intended for the manufacturing of structural components exposed to exceptionally high loads. The steel purchased was in the form of a bar of the diameter ∅ = 60 mm. Table 1 shows properties of the material of the bar manufactured at the Batory Steelworks according to the Engineering Acceptance Report No. 212/P/89, and specifications for the steel following the Polish Standard PN-72/H-84035.

Tab. 1. Properties of the material of the bar according to the Engineering Acceptance Report, and specifications following the Polish Standard PN-72/H-84035

Chemical composition [%]							
	C	Mn	Si	P_{max}	S_{max}	Cr	Ni
	0.28÷0.30	1.16	1.08	0.024	0.011	0.93	1.58
PN-72/H-84035	0.27÷0.34	1.00÷1.30	0.90÷1.20	0.030	0.025	0.90÷1.20	1.40÷1.80
Mechanical properties (after thermal treatment: quench hardening 900^0 C 20' oil, tempering 250^0 C 3 h air)							
	R_m [MPa]	R_e [MPa]	A [%]	Z [%]	$KCU2$ [J/cm^2]	HB	
	1725÷1775	1505÷1535	13÷14	45÷47	90÷95	2.8	
PN-72/H-84035	min. 1620	min. 1370	min. 9	min. 45	min. 60	-	

The following specimens were prepared for the tests:

- cylindrical ones for strength and static tensile testing,
- sand-clock ones for low-cycle fatigue (LCF) testing,
- cylindrical ones for high-cycle fatigue (HCF) testing,
- round compact tension (RCT) ones for testing both fatigue-crack propagation rate and crack toughness.

Shapes and dimensions of the specimens have been shown in Figs 1 ÷ 4.

The quench hardening was carried out in oil, starting from 900^0 C; the tempering was carried out at temperature ranging from 240 to 250^0 C for three hours. After that, the specimens were cooled in steady air. What followed the thermal treatment was grinding of the specimens.

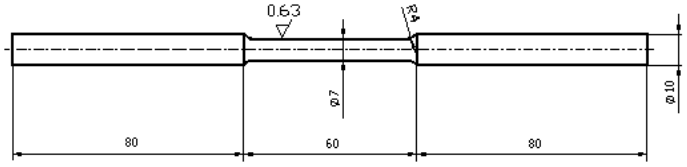

Fig. 1. Shape and dimensions of an exemplary specimen for strength testing

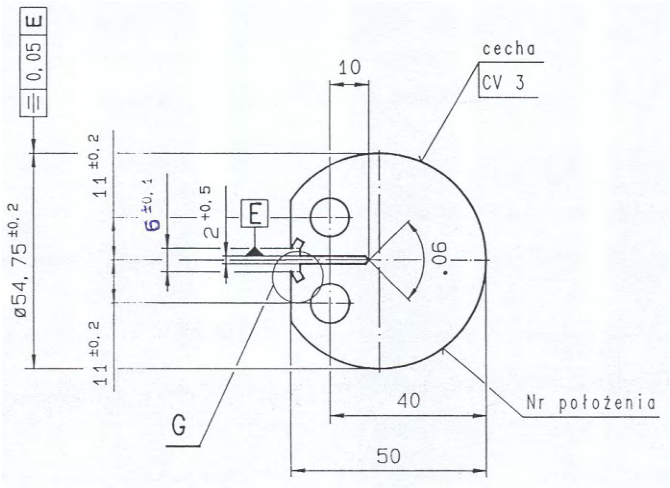

Fig. 2. Shapes and dimensions of specimens to examine fatigue-crack propagation rates and crack toughness

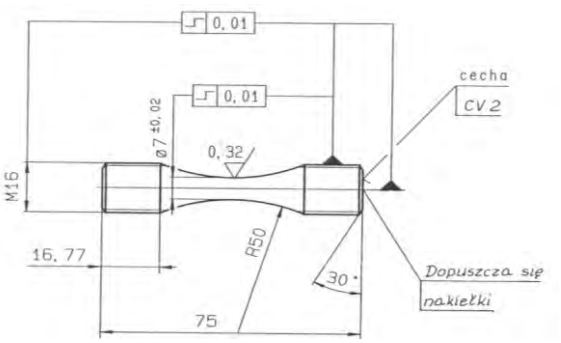

Fig. 3. Shapes and dimensions of specimens for low-cycle fatigue (LCF) testing

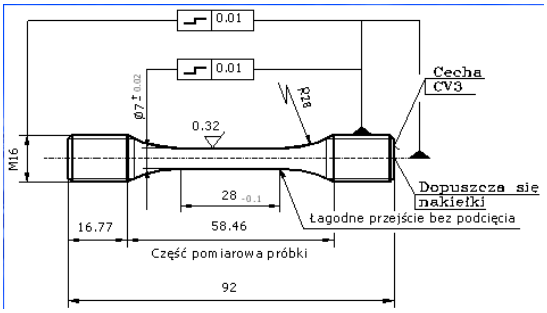

Fig. 4. Shapes and dimensions of specimens for high-cycle fatigue (HCF) testing

Findings on mechanical properties of the 30HGSNA steel

Sample	d_0	L_0	$R_{0,05}$	$R_{0,2}$	R_m	$R_{m\,rz}$	A	**n**	K	E
	[mm]	[mm]	[MPa]	[MPa]	[MPa]	[MPa]	[%]		[MPa]	[MPa]
2/05/1	6.95	50	420	450	795	910	-	**0.190**	1374	200600
2/05/2	6.78	50	1160	1340	1655	1695	-	**0.110**	2700	202300
2/05/3	6.85	50	1145	1325	1655	1700	-	**0.110**	2658	201100
2/05/4	6.83	50	1150	1315	1640	1685	-	**0.105**	2544	194000
2/05/5	6.80	50	1150	1320	1640	1685	-	**0.105**	2554	200200
2/05/36	7.92	30	1200	1360	1670	1730	13.7*	**0.100**	2552	197300
2/05/61	4.95	25	1230	1380	1700	1755	11.1	**0.090**	2467	199700
2/05/62	4.96	25	1230	1390	1700	1750	-	**0.090**	2475	197500
2/05/63	4.99	25	1240	1400	1715	1765	11.2	**0.090**	2484	198800
2/05/64	4.99	25	1175	1365	1715	1800	13.0	**0.100**	2508	198700
2/05/132	7.87	30	1175	1345	1670	1705	-	**0.100**	2483	206800
2/05/133	5.96	50	1235	1415	1750	1805	7.6**	**0.105**	2694	201600
2/05/134	5.98	50	1280	1430	1735	1785	7.5**	**0.090**	2497	198900
2/05/135	5.99	50	1290	1425	1730	1785	7.6**	**0.085**	2500	195500
2/05/136	5.98	50	1330	1450	1720	1760	7.4**	**0.080**	2441	197300
2/05/137	6.93	50	1220	1395	1730	1800	9.5**	**0.100**	2638	201800
2/05/138	6.79	50	1225	1400	1735	1800	9.0**	**0.090**	2526	194500
2/05/139	6.90	50	1235	1405	1730	1800	7.0**	**0.095**	2521	197700
2/05/140	5.76	50	1240	1400	1725	1780	8.1**	**0.105**	2690	207300
2/05/141	6.03	50	1225	1400	1720	1770	7.6**	**0.100**	2630	198000
2/05/142	5.84	50	1250	1410	1715	1770	7.7**	**0.090**	2511	203200

*A_{30mm}; **A_{50mm};

On the grounds of the conducted testing work it has been found that the mechanical properties of the 30HGSNA steel are as follows:

- offset yield strength $R_{0,05}$ = 1220 MPa ± 1.82%
- offset yield strength $R_{0,2}$ = 1385 MPa ± 1.24%
- rated tensile strength R_m = 1700 MPa ± 0.90%
- percentage elongation A = 12.2% ± 10.64%
- Young's modulus E = 199600 MPa± 0.80%
- true tensile strength $R_{m,rz}$ = 1755 MPa ± 0.34%
- static strain-hardening exponent n = 0.100 ± 3.60%
- static strength coefficient K = 2554 MPa ± 1.46%

All the values found are average values calculated with the expanded uncertainty of the average at the level of confidence 95%.

Results of strength tests carried out at AFIT have been verified under the Excellence Testing Project, with approximately 100 laboratories from all over Europe participating. The below-presented figures show the position of test results gained at AFIT against those obtained by other laboratories – AFIT has been encoded as Laboratory No.172.

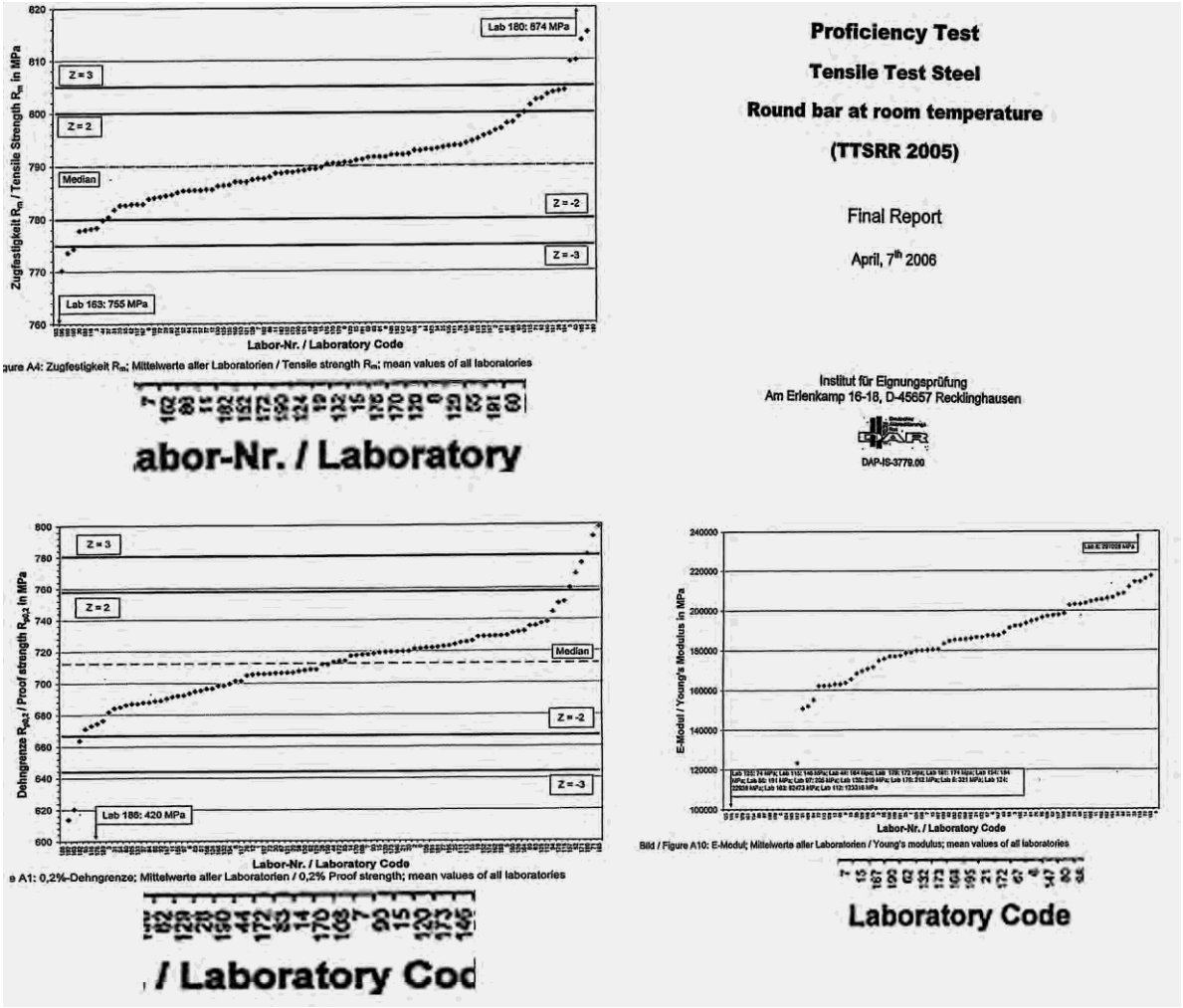

Fig.5. The Excellence Testing results.

Results of low-cycle fatigue tests

Tests that consist in the evaluation of fatigue life ($2N_f$) against deformation range ($\Delta\varepsilon$) have allowed of the determination of the curve $\Delta\varepsilon$-$2N_f$ (fig.6) using the Manson-Coffin equation of the following form:

$$\frac{\Delta\varepsilon}{2} = \frac{\Delta\varepsilon_{spr}}{2} + \frac{\Delta\varepsilon_{pl}}{2} = \varepsilon_f \left(2N_f\right)^a + \sigma_f \left(2N_f\right)^b$$

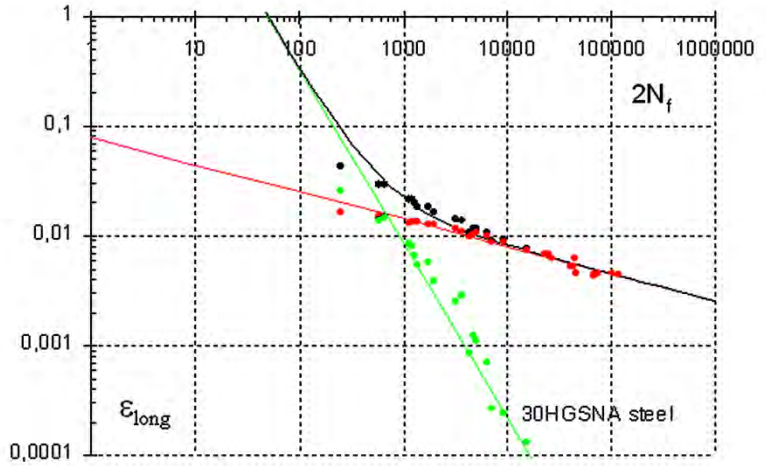

$$\frac{\Delta\varepsilon}{2} = \frac{\Delta\varepsilon_{spr}}{2} + \frac{\Delta\varepsilon_{pl}}{2} = 0{,}0791 \cdot \left(2N_f\right)^{-0{,}24855} + 477{,}07\left(2N_f\right)^{-1{,}58485}$$

Fig.6. Low-cycle fatigue results

Results of high-cycle fatigue tests

Tests that consist in the evaluation of fatigue life ($2N_f$) against the stress amplitude (σ_α) have allowed of the determination of the curve σ_α-$2N_f$ (fig.7) using the Morrow equation of the following form:

$$\sigma_a = \sigma_f^{'} \left(2N_f\right)^b$$

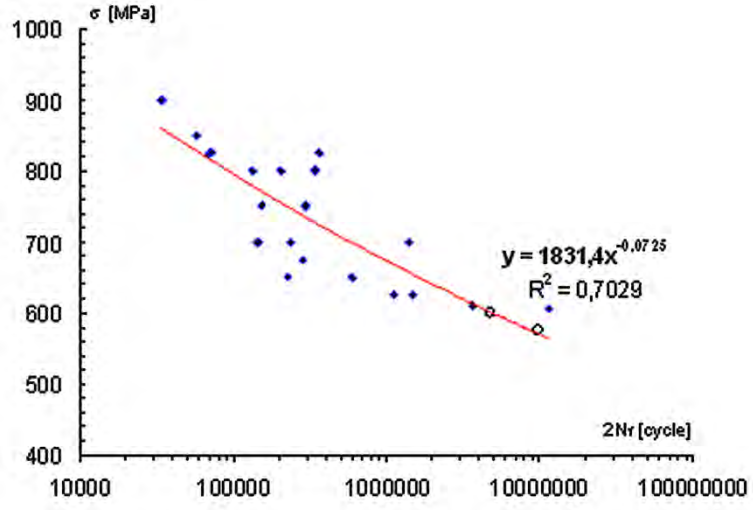

$$\sigma_a = 1831.4 \cdot \left(2N_f\right)^{0.0725}$$

Fig.7. High-cycle fatigue results

Results of constant-load-amplitude fatigue crack growth rate (FCGR) testing

Precracks of length up to a = 12.5 mm were produced in the specimens at $K_{końc}$ = 30 $MPa\sqrt{m}$. Determined were coefficients in the Paris and NASGRO equations that describe the propagation curves. The Paris equation has the following form:

$$\frac{da}{dN} = C(\Delta K)^m$$

Coefficients included therein allow of describing propagation curves for different stress intensity factor ranges ΔK (threshold, steady, critical ones) for individual specimens are presented in Table 4 (below).

Sample	*R*	*m*	*C*	Correlation coefficient	Regression range	
					da/dN min	*da/dN max*
2-05-71	0.10	2.856	1.8395E-08	0.9679	1.00E-05	1.00E-04
2-05-71	0.10	2.814	1.8719E-08	0.9948	6.00E-04	1.00E-05
2-05-66	0.05	2.750	2.1755E-08	0.9969	1.00E-06	3.00E-04
2-05-66	0.05	2.803	1.7778E-08	0.9664	2.00E-06	5.00E-04
2-05-65	0.05	2.661	2.8916E-08	0.9936	2.40E-06	5.20E-04
2-05-124	0.10	2.816	1.9258E-08	0.9927	7.00E-06	2.00E-04
2-05-119	0.10	3.015	9.3170E-09	0.9963	2.00E-06	3.50E-04
2-05-77	0.10	2.804	1.9788E-08	0.9871	1.50E-05	1.00E-03
2-05-119	0.10	2.921	1.1330E-08	0.9969	2.00E-05	7.00E-04
2-05-120	0.09	3.321	2.4786E-09	0.9970	1.00E-06	1.10E-04
2-05-76	0.10	3.019	8.5387E-09	0.9905	5.00E-06	3.00E-04
2-05-124	0.10	2.741	2.1695E-08	0.9901	7.00E-05	1.00E-03
2-05-77	0.10	8.048	4.7262E-17	0.9359	7.00E-04	2.30E-02
2-05-119	0.10	8.490	9.4914E-18	0.9037	7.00E-04	1.00E-02
2-05-77	0.10	9.371	2.5037E-19	0.9522	1.00E-03	2.30E-02
2-05-124	0.10	7.113	9.4344E-16	0.9565	1.00E-03	4.00E-02
2-05-76	0.10	9.212	3.3835E-19	0.8817	1.00E-03	1.00E-02
2-05-119	0.50	2.771	2.7158E-08	0.9891	1.00E-06	7.00E-05
2-05-72	0.50	2.915	2.2405E-08	0.9788	4.30E-06	1.00E-04
2-05-73	0.50	2.659	3.8849E-08	0.9777	1.00E-06	3.00E-05
2-05-120	0.50	3.346	4.2326E-09	0.9912	1.00E-06	6.00E-05
2-05-124	0.50	2.828	2.4071E-08	0.9912	2.60E-06	1.00E-04
2-05-73	0.50	3.185	1.0225E-08	0.9936	1.00E-05	3.00E-04
2-05-84	0.50	3.517	4.0724E-09	0.9556	5.00E-04	1.00E-02
2-05-72	0.50	3.040	1.5690E-08	0.9918	4.00E-04	4.00E-03
2-05-84	0.50	9.128	3.1555E-17	0.4794	5.00E-04	1.00E-02
2-05-72	0.50	8.397	4.0201E-16	0.7342	4.30E-06	4.00E-04
2-05-74	0.80	3.215	2.1108E-08	0.9380	1.00E-06	1.00E-05
2-05-74	0.80	2.848	3.6587E-08	0.9563	1.20E-06	1.50E-05
2-05-120	0.80	3.995	2.1848E-09	0.9237	1.60E-06	8.00E-05
2-05-67	0.80	2.910	3.2668E-08	0.9456	2.40E-06	4.00E-05
2-05-78	0.80	3.310	1.5736E-08	0.9406	3.60E-06	1.00E-04
2-05-79	0.80	4.165	2.3139E-09	0.9341	3.80E-06	1.00E-04
2-05-124	0.80	3.017	2.5941E-08	0.9151	9.00E-06	4.60E-05
2-05-67	0.80	11.886	1.2537E-17	0.8216	4.00E-05	7.00E-03
2-05-78	0.80	9.644	5.0882E-15	0.6991	5.25E-05	4.00E-03
2-05-78	0.80	8.333	1.7890E-13	0.4519	1.00E-04	4.00E-03
2-05-79	0.80	10.984	1.9669E-16	0.6991	1.00E-04	4.20E-03
2-05-79	0.80	9.587	6.8176E-15	0.7344	5.25E-05	4.20E-03

Since the Paris equation takes no account of the dependence of crack propagation curves on the stress ratio R, a relationship between values of coefficients C and m for particular curves was found, i.e. for test results gained at R = 0.1; 0.5; and 0.8 – see fig. 8.

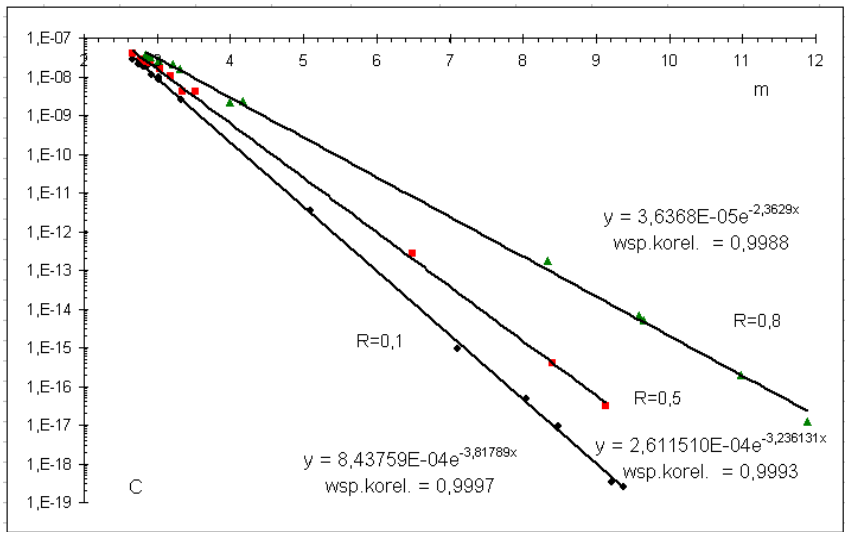

Fig. 8. Relationship between values of coefficients C and m for particular curves (i.e. for test results gained at R = 0.1; 0.5; and 0.8)

The relationships between the C and m coefficients and R (for tests conducted at different stress ratios R) in the semi-log coordinate system are linear and described with equations of the following type:

$$C = a_{1,R} e^{a_{2,R} m}$$

where coefficients $a_{1,R}$ and $a_{2,R}$ take values as shown in Fig. 8.

In specific cases the Paris equation takes the following forms:

- for R = 0.1 $$\frac{da}{dN} = \left(8.438 \cdot 10^{-4}\right) e^{(-3.818)m} \left(\Delta K\right)^m$$
- for R = 0.5 $$\frac{da}{dN} = \left(2.612 \cdot 10^{-4}\right) e^{(-3.236)m} \left(\Delta K\right)^m$$
- for R = 0.8 $$\frac{da}{dN} = \left(3.637 \cdot 10^{-5}\right) e^{(-2.363)m} \left(\Delta K\right)^m$$

Since there are linear relationship between both the coefficients, i.e. $a_{1,R}$ and $a_{2,R}$, and the stress ratio R, a generalized form of the Paris equation for a given material can be written down:

$$\frac{da}{dN} = \left(9.26 \cdot 10^{-4} - 1.17 \cdot 10^{-3} R\right) e^{(-4.093+2.045R)m} \left(\Delta K\right)^m$$

It means that if some pre-set value of the m coefficient in the Paris equation is taken from some specific range of ΔK, the value of the C coefficient can be calculated from the above written equation – within the range of the stress ratio R changing from 0.1 to 0.8.

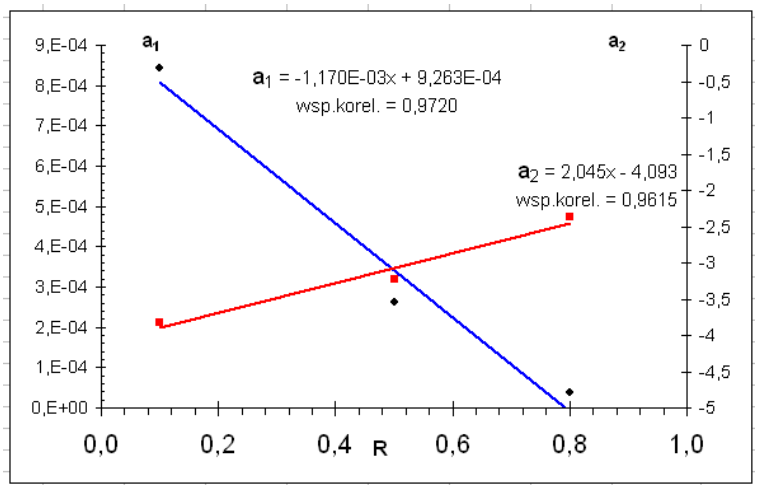

Fig. 9. How values of $a_{1,R}$ and $a_{2,R}$ coefficients depend on stress ratio R

The NASGRO equation (by Forman & Newman from NASA, de Koning from NLR, and Henriksen from ESA) takes the following form:

$$\frac{da}{dN} = C\left[\left(\frac{1-f}{1-R}\right)\Delta K\right]^n \frac{\left(1-\frac{\Delta K_{th}}{\Delta K}\right)^p}{\left(1-\frac{K_{\max}}{K_{crit}}\right)^q}$$

where:

$$f = \frac{K_{op}}{K_{\max}} = \begin{cases} \max\left(R, A_0 + A_1 R + A_2 R^2 + A_3 R^3\right) & R \geq 0 \\ A_0 + A_1 R & -2 \leq R < 0 \\ A_0 - 2A_1 & R < -2 \end{cases}$$

$$A_0 = \left(0.825 - 0.34\alpha + 0.05\alpha^2\right)\left[\cos\left(\tfrac{\pi}{2} S_{\max}/\sigma_0\right)\right]^{1/\alpha}$$

$$A_1 = \left(0.415 - 0.071\alpha\right) S_{\max}/\sigma_0$$

$$A_2 = 1 - A_0 - A_1 - A_3$$

$$A_3 = 2A_0 + A_1 - 1$$

and

$$\Delta K_{th} = \Delta K_0 \left(\frac{a}{a + a_0}\right)^{1/2} \Big/ \left(\frac{1-f}{(1-A_0)(1-R)}\right)^{(1+C_{th}R)}$$

a – initial crack length,
a_o – detectable crack length (0.0015” or 0.0000381m),
α – stress-state-dependent constraint factor,
S_{max}/σ_o – the maximum-applied-load–*to*–yield-stress ratio,
C_{th} – slope of the propagation curve within threshold range,
K_{Ic} – crack toughness (mode I),
ΔK_o – threshold stress intensity factor for $R = 0$ (ΔK_{th} for $R = 0$),
t – thickness of the specimen,
t_o – reference thickness of the specimen for the plane state of strain
A_k, B_k – matching parameters,

with the plane-state-of-strain condition satisfied:

$$t_0 = 2.5\left(K_k/\sigma_{ys}\right)^2$$

and with the asymptotic convergence of K_{crit} and K_{Ic}, if the specimen thickness exceeds the t_0:

$$K_{crit}\Big/K_{Ic} = 1 + B_k e^{-\left(A_k\, t/t_0\right)^2}$$

Coefficients in the NASGRO equation, which describe the plotted propagation curves, have the following values:

K_{crit}	α	S_{max}/σ_o	ΔK_o	a	C_{th}	C	n	p	q
79	2.5	0.3	4.4	0.0125	0.2	4.9E-11	2.54	0.25	1

Fig. 10. shows degrees of matching these propagation curves to experimental data.

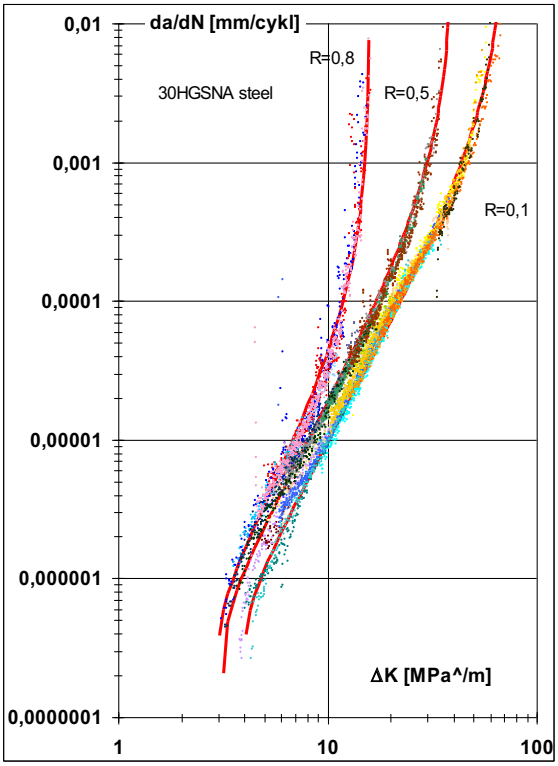

Fig. 10. Fatigue crack growth rates as plotted for different stress ratios R = 0.1; 0.5; 0.8

Results of testing crack resistance under plane-state-of-strain conditions

Test samples to examine the material's crack resistance were cut in the direction transverse to the bar axis (fig.11). The testing of crack resistance under plane-state-of-strain conditions were carried out using the testing machine MTS 810.23. Round compact tension (RCT) specimens of W = 40 mm and B = 7 mm were subjected to tests. Precracks of lengths up to a = 20 mm were produced in the specimens at $K_{końc}$ = 30 $MPa\sqrt{m}$.

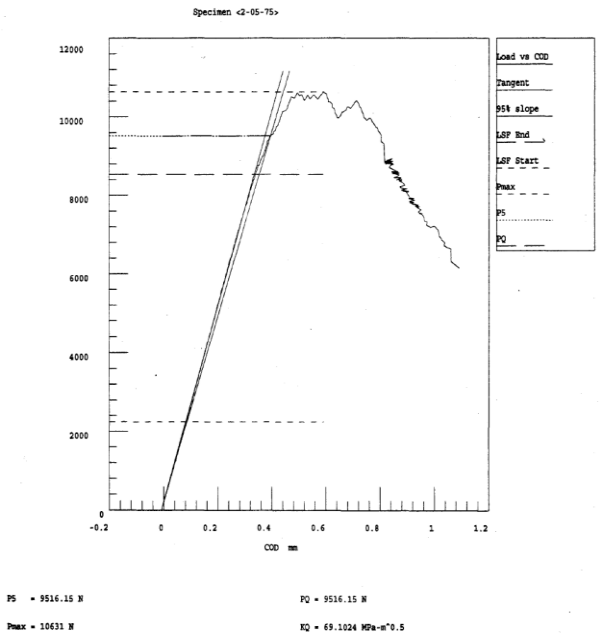

Fig. 11. An exemplary curve resulting from testing the crack resistance under plane-state-of-strain conditions

The average found from test results is 69.8 $MPa\sqrt{m}$ .Uncertainty of the average is U = ±4.36% at the level of confidence 95% and coverage factor k_p = 2.87.

The test results satisfy all the criteria provided in the ASTM E 399 standard.

CONCLUSIONS

1. Values of the yield strength and crack resistance gained from the tests on cylindrical specimens made of the 30HGSNA steel satisfy requirements of the PN-72/H-84035 standard and exceed the required ones by approximately 1.5% and 5 %, respectively. The Young's modulus found for this steel is E = 199300 MPa.
2. The low-cycle fatigue (LCF) tests carried out using sand-clock specimens made of the 30HGSNA steel, 7 mm in diameter, with the PN-84/H-04334 and ASTM E-606 standards followed, allow of the determination of the Manson-Coffin curve for this steel, which takes the following form:

$$\frac{\Delta\varepsilon}{2} = \frac{\Delta\varepsilon_{spr}}{2} + \frac{\Delta\varepsilon_{pl}}{2} = 0.0791 \cdot \left(2N_f\right)^{-0.24855} + 477.07\left(2N_f\right)^{-1.58485}$$

   Because of the sizes of pre-set (in the tests) ranges of strain $\Delta\varepsilon$, and experimentally gained strength of specimens $2N_f$, the above-mentioned relationship can be applied for the number of cycles N_f ranging from $3\cdot10^2$ up to10^6.
   For strength below the number of cycles $3\cdot10^2$, values of the σ_f and b coefficients will change considerably. Evaluation thereof requires additional testing work at very large plastic ranges.
3. The crack resistance of the 30HGSNA steel K_{1c} is 69.8 $MPa\sqrt{m}$.

4.2 Experimental and Theoretical Investigations of Fatigue Crack Growth in D16 Alloy

(Lucjan Śnieżek – Military University of Technology, Warsaw)

In this work, the arising and development of fatigue crack in aluminium alloy D16, taking into consideration the influence of the notch in the form of a hole with side incisions were tested. The test programme was developed based on prior numeric analysis of the stresses pattern and strains distribution in the zone of the notch's influence, focused on determination of stresses face values. To examine stress and strain distributions, the specialised FEM software (MSC Patran and MSC Nastran) was applied. Findings have been presented in the form of a statement of σ_{max} and ε_{max} values, and functions of the following factors: a_σ, a_ε and a_k, computed based on these values for both different distances from the bottom of the notch and the assumed levels of loading the specimens.

Theoretical analysis has been supplemented with experimental investigation into the microstructure of fatigue-fracture surfaces in the area of crack initiation and that of fatigue of a the propagating crack. The work has been intended to present a model of the probabilistic estimation of fatigue life of structural members. The model has been based on the deterministic description of the cracking. Analyzed were components with notches in the form of centrally located holes with side cuts.

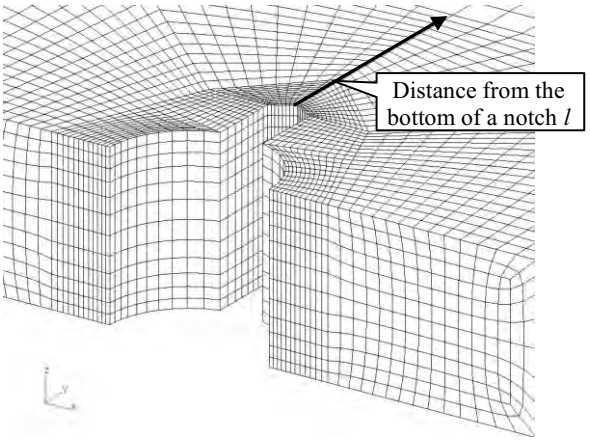

Fig. 1. A discrete FEM model assumed for analysis

In the method of probabilistically approaching the crack propagation, some dependences have been used that take account of the presence of areas showing plastic strains in front of crack tips. It has been assumed that the cracking can be modeled on the basis of some general-purpose quantity used to describe the energy state in the area of the crack tip, i.e. the Rice's integral (J). The formulated computational model has been used to estimate fatigue life of model components made of D16 alloy. Experimental work was carried out using some flat specimens with centrally positioned holes. They were exposed to flat bending at R = 0. Analytical and experimental results have shown a high degree of consistency.

4.3 The Effect of a Complex Stress State on Fatigue Crack Propagation and the Orientation of the Cracking Plane in VT3-1 Aeronautical Titanium Alloy

(Janusz Mierzyński – Military University of Technology, Warsaw)

The results of titanium alloy fatigue crack tests have been published for many years. This is due to the wide use of titanium alloys in structures, in which there is needed a high ratio of material strength to a component's weight.

Titanium alloys show a wide diversity of fatigue properties, which results from the diversity in their chemical composition and structure. Production technology as well as the type and conditions of heat treatment play a great role in attaining suitable mechanical and fatigue properties of the alloys. The size of grains in titanium alloys shows an exceptionally high range, namely from 5 to 1000 μm. They have a significant effect on the propagation of cracks, especially short ones, owing to crack arrest effects at grain boundaries. There are different crack initiation mechanisms in α-phase (a hexagonal system) and β-phase (a body-centered cubic system), which the VT3-1 titanium alloy consists of. Generally speaking, gaining knowledge of the crack growth rate in multicomponent titanium alloys requires familiarizing oneself with specific publications, since it is difficult to formulate any general conclusions.

In the study, much attention was paid to the propagation of short fatigue cracks in the VT3-1 alloy. The term "short cracks" indicates cracks which propagate at the initial stage of fatigue changes in a structural material. The length of these cracks does not exceed the threshold length l_{th}, which is conditioned by the size of material grains. Short cracks propagate below the threshold value of the stress intensity factor K_{th}. Above these threshold values, there propagate long cracks, the growth of which has to be controlled during the operating period of a structural component, since they may cause the complete destruction of a component. Therefore, the range of short crack propagation constitutes the safe operating period of components.

In the work, particular emphasis was placed on indicating short fatigue cracks in the VT3 - 1 alloy, determining the effect of load conditions on the change of the orientation of the cracking plane as well as the correlating the features of crack growth behaviour with the features of the microstructure of fractured surfaces. Detailed results of the research were presented for the ratios of the torsional moment M_t to the bending moment M_b such as $M_t/M_b = 2.25$, $M_t/M_b = 1$ and $M_t/M_b = 0.5$. It was crucial to determine the fatigue strength range, in which short cracks propagate, as well as the range of the lengths of short cracks, which is of great importance in formulating deterministic and probabilistic descriptions of the dynamics of fatigue cracking of components. The aim was to obtain a complete picture of fatigue crack development.

There was investigated the effect of a complex state of stress on the propagation of both short and long fatigue cracks as well as on the orientation of the cracking plane in VT3-1 titanium alloy components with circumferential notches, at different ratios of the torsional to the bending moments. The presence of a range of the growth of short fatigue cracks at a limited range of stresses was noticed. Characteristic behaviour of short fatigue cracks initiated on the circumference of the notch surface was observed. A characteristic feature was the irregularity in the propagation of short cracks, which was caused by the strong influence of the material structure. The aforementioned irregularities in crack propagation were reflected in crack growth rate diagrams. A high initial growth rate of short cracks in specimens was attributed to the possible effect of atmospheric hydrogen that penetrated the sides of cracks during fatigue tests. The depth of hydrogen penetration corresponded to the depth of the occurrence of brittle cracking,

fissile cracking and cracking along α-phase boundaries in the VT3-1 alloy. The range of the propagation of short surface cracks under bending loads was from 150 to 400 μm, whereas under combined bending and torsional loads it ranged from 50 to 400 μm. The range of the occurrence of short cracks in the VT3-1 titanium alloy may be even up to 60% of a component fatigue life. The features characteristic of the analyzed cracks were not noticed at high stresses. A significant influence of the VT3-1 alloy structure on the propagation of cracks was observed. In the case of an alloy of lamellar structure tested at $M_t=0.5M_b$, no signs of short fatigue cracks were found in any stress range. The angle of the inclination of the fracture plane to the specimen axis was changing depending on load conditions. The orientation of these planes was approximate to the orientation of the planes of the principal stresses at the point of maximum material effort at the notch bottom. At combined bending and torsional moments, where $M_t=0.5M_b$, the angle was in the range of 72°÷79°. At $M_t=M_b$, the angle of the inclination of the planes of specimen fractures was smaller, namely 62°÷67°. Increasing the contribution of the torsional moment in relation to the bending moment up to the ratio $M_t/M_b=2.25$ resulted in the situation where the planes of specimen fractures were inclined to specimen axes at the angles of 50° to 61°.

Research results constitute an experimental base for an analytical description of the fatigue crack growth rates of components, in terms of short and long cracks, as well as predicting the orientation of the entire crack plane of a component under complex loads.

4.4 Deterministic Approach to Predicting the Fatigue Crack Growth in the 2024-T3 Aluminium Alloy under Variable Amplitude Loading

(Dorota Kocańda – Military University of Technology, Warsaw)

The results obtained from the experimental research on the fatigue crack growth rate both on the surface and inside the sheet of the 2024-T3 aluminum alloy under the LHL-100 block program loading with multiple overload-underload cycles, were utilized to check the ability of the proposed deterministic approach to predict crack growth.

In this approach, the modified Willenborg retardation model was applied. The microfractographic analysis of fatigue fracture of the CCT sheet specimens with the use of TEM (Transmission Electron Microscope) made it possible to trace the effect of block program loading on the crack growth rate. To assess the equivalent loading for the LHL block program the existing knowledge of the affectation of a particular overload-underload cycle or a block of these cycles on crack rate on the basis of microfractographic analysis was utilized. The crack growth rate inside the sheet was determined on the basis of fatigue striation spacing on the fracture surface of the CCT-type specimens. The microfractographic analysis proved that under the LHL-100 loading program, the crack propagates approximately for the time that corresponds to 4.2% of the spectrum operation. For a considerable time, the crack does not grow or it propagates at a very low rate. This behaviour of crack growth resulted from the affectation of the plastic zones created by the block of cycles of the highest stress level. The calculated crack growth rate was consistent with the experimentally determined crack growth rate.

4.5 Capacity of Fractographic Analysis for Load-Time History Reconstruction and Fatigue Crack Growth Rate Estimation for the 2024-T3 Aluminium Alloy

(Zdzisław Bogdanowicz – Military University of Technology, Warsaw)

The aim of this work was to present the considerations for the feasibility of load time history reconstruction on the basis of microfracture analysis for a failed component made of 2024-T3 aluminium alloy that operates under variable amplitude loading. For this goal, three different variable amplitude load sequences with single and multiple overloads and underloads were applied to investigate crack growth rate and to examine the images of fatigue striations on the fracture surface of a component. These loads are employed when simulating the fatigue crack behaviour in aeronautical alloys. Microfracture analysis was also used either for studying the interaction of variable amplitude loading for crack growth rate in 2024-T3 alloy or for establishing the relation between surface crack and crack depth growth.

Three load sequences were considered, namely simple OVL load program, the FBF (flight-by-flight) cycles sequence and LHL-100 block program, which differed in terms of the ordering and the number of various magnitude overloads or spike overload and underload cycles. The results indicate that the first overload-underload cycle in the sequence of either the FBF or the LHL-100 loads plays a very important role. One high spike overload and underload cycle in the FBF sequence more reduces the effect of crack retardation to a higher degree than the block with ten immediately following spike overloads-underloads in the LHL-100 program. As a result, the lifetimes of the specimens tested under the FBF loading are lower than those under the LHL-100 block program. The research proves the feasibility of load time history reconstruction of a failed component operated under simple loading like as OVL load program. The research also proves that short return periods occurring in the variable amplitude loadings with a certain number of immediately following spike overload-underload cycles present the limitation for doing the reconstruction of the load-time history on the basis of microfracture analysis.

5. JOINTS

5.1 Methods for FEM Analysis of Riveted Joints of Thin-Walled Aircraft Structures with Submodelling Technique.

(Wojciech Wronicz – Institute of Aviation, Warsaw)

Riveting still remains the most popular method of joining metal parts of the aircraft structure. During the riveting process and the operation the severe stress concentrations and the effects such as fretting and secondary bending occur, thus reducing fatigue life. Riveting joints quality is influenced by structure and material as well as technological factors. They have a very strong influence on fatigue life. In the literature there are many works devoted to this subject, e.g. between 1993-1998 in Sweden a wide research program focused on joints was carried out. Among other, influence of type of joining elements (rivets and screwed elements) was studied. Fatigue life of specimens varied between 109 217 and 6730 flights, depending on element type. The research programme in Netherlands resulted in many PhD theses, e.g. Muller examined three row riveted lap joint and showed that, only by increasing force during riveting process, fatigue life can change from 39 630 cycles (minimal force) through 95 200 (nominal force) to 446 413 cycles (high force). Other works are devoted to influence of coating layers (clad, anode) on fatigue life.

Although the literature on the fatigue behaviour of riveted joints is quite abundant, many aspects are still not sufficiently understood and investigated and, therefore, they require a further study. Moreover most of them do not concerns types of rivets and sheets used in Poland. The goal of the Eureka-IMPERJA project is to increase fatigue life. This objective is met by investigating and improving the riveting process as well as improving prediction methods for fatigue life. The project refers to a real structure. One of the IMPERJA consortium partners, PZL Mielec, recommended its product, an airplane M28 Skytruck, as the object of investigations and analyses. In the IMPERJA programme, the study of FEM methodology modelling of the structure at three different complexity levels was planned: complete structure, structural detail and single riveted joint. The key issue of the proposed approach will be defining the rules of transferring the excitation (loading and boundary conditions) for the above modelling path.

Fig. 1. PZL M28 Skytruck

The PZL M28 Skytruck is a two-engined, braced high-wing monoplane for passenger/cargo transportation purpose with metal structure. The maximum take-off weight is 7500 kg. The aircraft has short take-off and landing (STOL) capability and can operate from short, unprepared runways. It is manufactured by PZL Mielec, and it is used by e.g. Polish Army, Polish Border Guard as well as customers from USA, Venezuela, Columbia, Vietnam, Indonesia and Nepal. It is a semi mono-cook metal structure. The airplane wing consists of a rectangle centre wing and two trapezium outer wing parts.

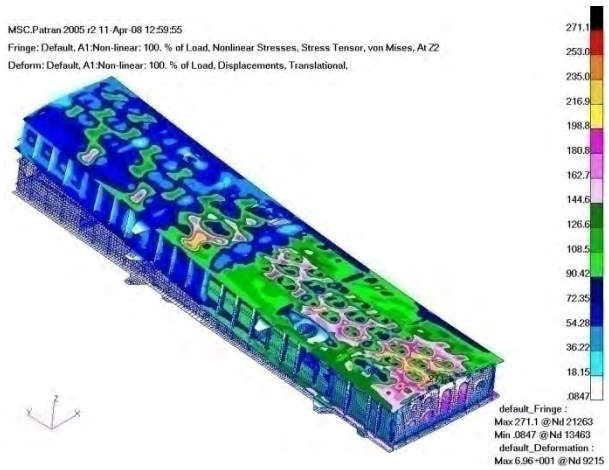

The aim of the work was to analyze low skin riveted joint near rib no 21 on the PZL M28 Skytruck wing. First, global model includes three bulkheads on each side of rib no 21, i.e. part between ribs no 18 and 24. The model was used to gain boundary conditions for more accurate models. Rivets were not represented. Shell elements and linear material models were used. The boundary conditions were taken based on the operational data.

Fig. 2. Equivalent stresses (Huber Mises Hencky) and displacements of the model

A fragment of the bottom skin, near rib no 21 was chosen for local I level analysis. The riveted joint FEM model was built for this region. Dimensions of the model are 400 x 150 mm. Shell elements were used. The presence of the rivet was taken into account, as well as the distance between middle surfaces of jointed parts. Boundary conditions (forces) were set based on global model calculation. Previous analyses showed that in submodelling technique, in the case of significant flexibility difference between models, it is better to use forces instead of displacements as boundary conditions. Residual stresses connected with riveted process were modelled using temperature and thermal coefficient. Nonlinear material model was used. Figure 2 presents equivalent stresses and displacements obtained in the analysis.

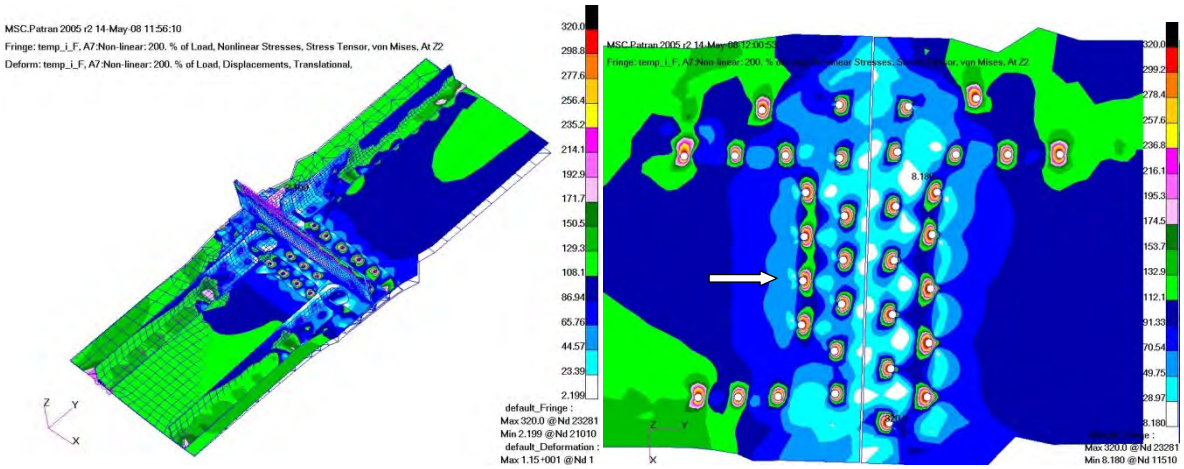

Fig. 3. Equivalent stresses and displacements of the local I level model

Rivet marked with an arrow on fig. 3 was chosen for local II level analysis.

The Solid model of the chosen rivet was built. It covers the fragment (square of 12 mm side) of skin and doubler with the rivet. Nonlinear material models were used. Loads were applied in two stages. In the first stage residual stresses were inducted (using temperature and thermal coefficient). In the second stage external loads were added based on riveted joint model calculation. Results of the analyses are presented on fig. 4.

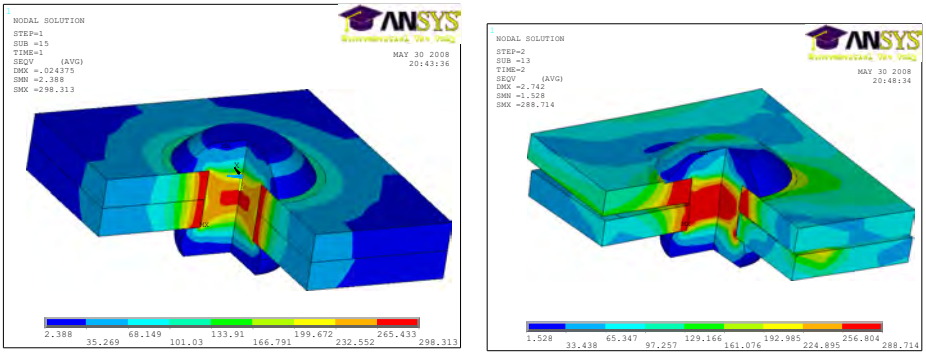

Fig. 4. Equivalent stresses (Huber Mises Hencky) and displacements after I (left) and II (right) stage. Displacements multiplied10 times.

Obtained stresses after I stage were compared with results from PhD thesis of Mr. Muller from TU Delft, who performed numerical simulation of riveting process. It is presented on fig. 5-6.

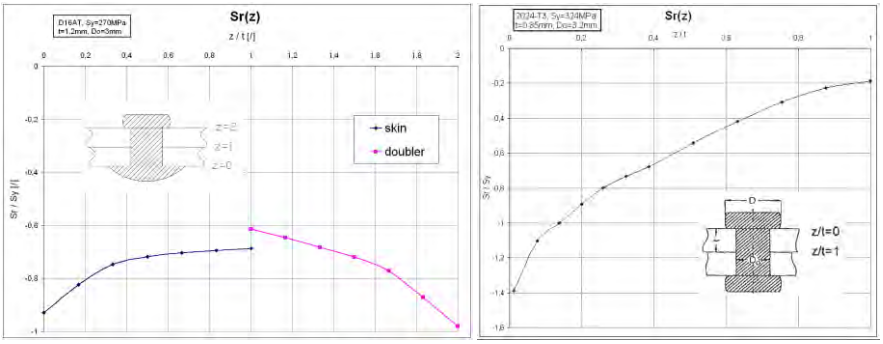

Fig. 5. Residual radial stresses through the thickness on the edge of the hole; left) at present work, right) based on PhD thesis of Mr. Muller

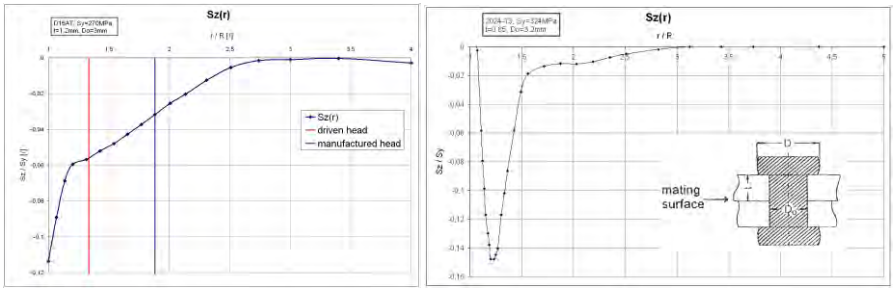

Fig. 6. Residual axial stresses at the mating surface; left – at present work, right – based on PhD thesis of Mr. Muller

The results indicate small accuracy of presented method of residual stresses modelling. It's not good enough for the detail analysis of riveting process, but could be useful in bigger models including a few or even several dozen rivets.

The analysis was performed for the solid mushroom rivet (shank diameter 3,5 mm) joining two aluminium sheets (thickness 1,2 mm). The three-dimensional numerical model of the neighbourhood (10,5 mm wide) of a single rivet was considered. Solid elements and nonlinear material model were used. Riveted joint deformations are shown in fig. 7. Radial land equivalent stresses are presented in fig. 8-9.

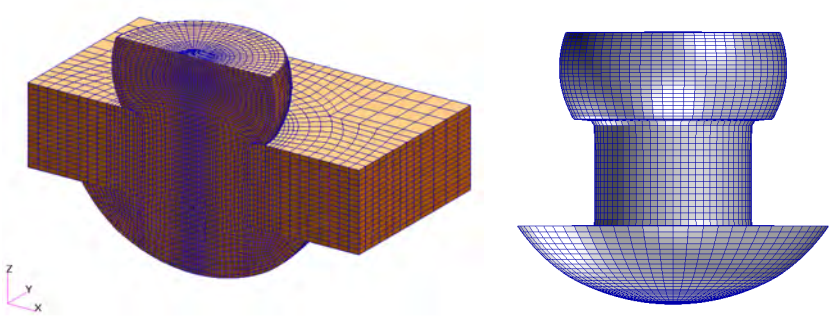

Fig. 7. Riveted joint deformations after upsetting

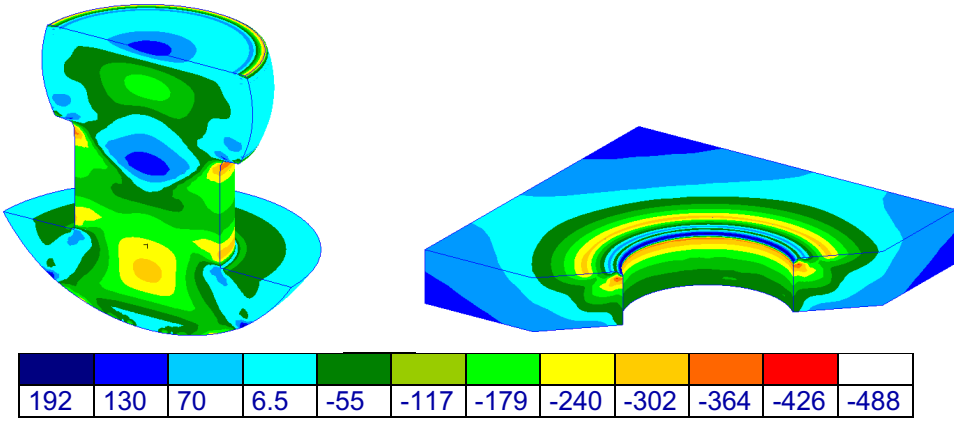

Fig. 8. Radial stresses in rivet and sheet after unloading

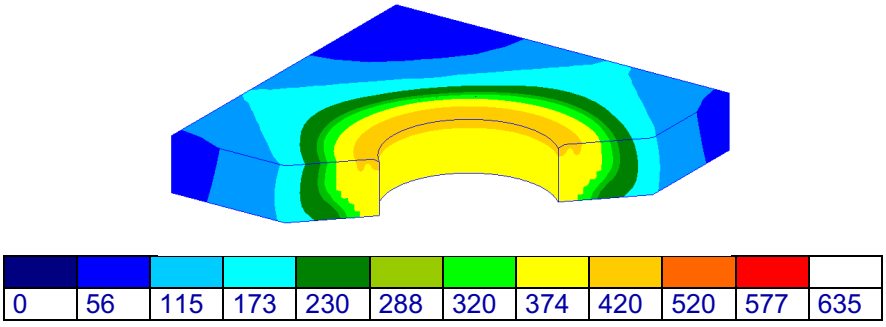

Fig. 9. Equivalent stresses in sheets during riveting (pressing stage)

The work presents the current state of the work. The riveted joint was analyzed at three levels with submodelling technique. The model of a single rivet turned out to be too simple and not accurate enough. A more precise model (simulation of riveting process) was developed. The next step will be to analyze the model of a rivet with compensator and load it with boundary conditions from riveted joint analysis.

5.2 Stress Measurements Around Rivets with X-ray Diffractometry

(Elżbieta Gadalińska – Institute of Aviation, Warsaw)

X-ray diffractometry serves as a one of a number of methods for residual stress evaluation. The essential advantage of this method is that it is accurate and absolute. The diffraction of X-rays on a crystal lattice of a copper sulphate was detected by Max von Laue in 1912. The mathematical formula for this phenomenon was expressed by William Bragg and it is as follows:

$$n\lambda = 2d \sin\theta \tag{1}$$

where:

n - is an integer determined by the order given,
λ - is the wavelength of diffracting X-ray,
d - is the spacing between the planes in the atomic lattice,
$\sin\theta$ - is the angle between the incident ray and the scattering planes.

The formula shows that the diffraction will occur only for unique Bragg's angles. Since its publication in 1913 the Bragg's law has been a powerful tool for studying crystals' structure. One of its applications is the residual stress measurement. The formula for stress calculation in a crystal is as follows:

$$\sigma_\varphi = \left(\frac{E}{1+\nu}\right)_{hkl} \frac{1}{d_0}\left(\frac{\partial d_{\varphi\psi}}{\partial \sin^2\psi}\right) \tag{2}$$

All the stress measurement results presented here were obtained using a Stresstech Oy built X-ray diffractometer model Xstress3000. It is a mobile device capable of performing measurements in two modes: ψ and Ω, with Φ rotation and Ψ and Φ oscillation. There is a set of collimators from the 0,5mm diameter to 5mm. This equipment is fully automated with a software controlled X-Y table for sequential measurements at a programmable set of points with given X-Y coordinates. The purpose of this study was to determine the residual stress distribution around the rivets and compare it with the FEM analysis performed by R.P.G. Müller in his Ph.D thesis [1].

SPECIMENS

Four types of specimen were used:

1. Large specimens – metal sheets made of D16CzATV alloy, 2mm thick; rivets made according to the standard OST 1 34040 – mushroom head rivets with the compensator.
2. Small specimens – made of D16AT alloy, 1.2mm thick sheet; rivets made of W65 alloy, according to the Russian standard ANU 0301 – countersunk rivets with the compensator.
3. Specimens made of rivet wire (two types: 3,5mm and 5mm diameter) after different treatment:
    - 1: polished with abrasive paper grade 100
    - 2: polished with abrasive paper grade 100, and then 280
    - 3: polished as 2, and then grade 600
    - 4: polished as 3, and then grade 1000
    - 5: polished as 4 and polished with diamond paste, grain size 3 μm
    - 6: polished as 5, and then polished electrolytically for 15 sec.

4. Specimen of a clad and anodized plate with three measurement areas: (1) original plate, (2) after removing the anodized layer with diamond paste, (3) after removing the anodized layer and cladding with abrasive paper grade from 280 to 800 and diamond paste, grain 3 μm.

FEM ANALYSIS RESULTS

The first series of results obtained from FEM analysis by R.P.G Müller predicted the stress distribution on the mating surface, for rivets with a driven head on both sides (for radial and tangential stresses) and for countersunk rivets (for tangential stresses only).

The second series of results predicted the stress distribution through the thickness at the edge of the hole for rivets with a driven head on both sides (radial stresses only) and for countersunk rivets (radial and tangential stresses).

Measurements were performed at Stresstech Oy on the surface of the specimens so the comparison of the measurement results and the FEM analysis results is limited. For every specimen the appropriate value D/D_0 is 1,5.

RESULTS OF X-RAY DIFFRACTION MEASUREMENTS

The X-ray measurements were performed on the surface of the specimen, on the side with the machined rivet head. The measurements were performed in radial (phi=0) and tangential directions (phi=90°). The anodized layer and the cladding were not removed before measurement.

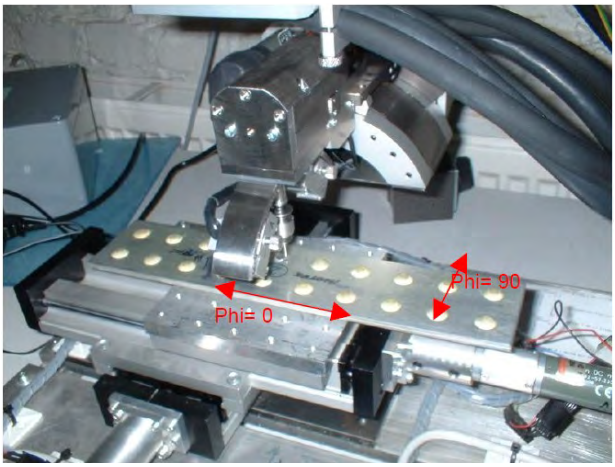

Photo 1: Large specimen during the measurement. Directions of measured stresses.

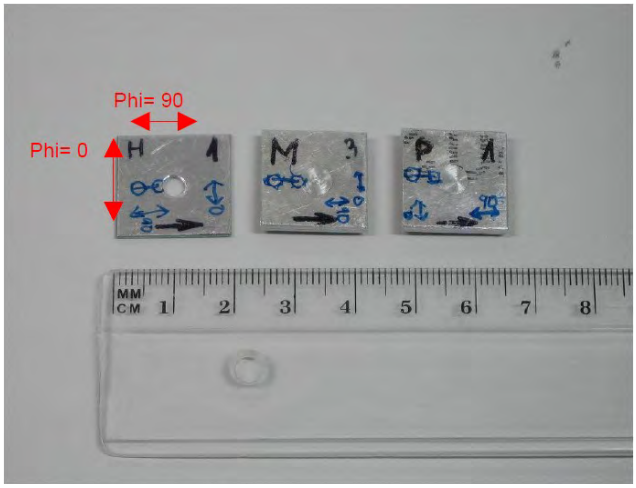

Photo 2: Small specimens. Directions of measured stresses.

Results are presented below:

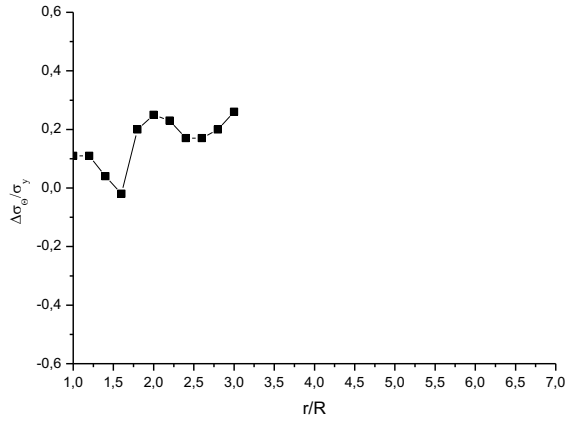

Fig. 1. The tangential stresses increment $\Delta\sigma_\theta$ on the surface of the specimen on the side with the machined rivet head (large specimen).

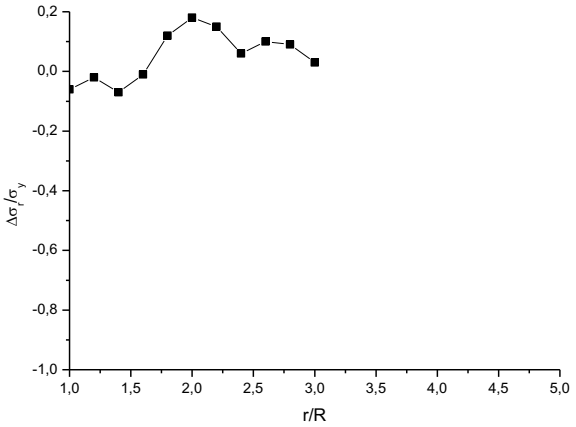

Fig. 2. The radial stresses increment $\Delta\sigma_r$ on the surface of the specimen on the side with the machined rivet head (large specimen).

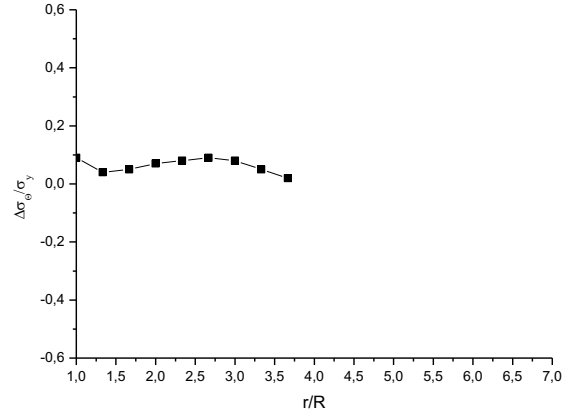

Fig. 3. The tangential stresses increment $\Delta\sigma_\theta$ on the surface of the specimen on the side with the machined rivet head (small specimen riveted manually: M3).

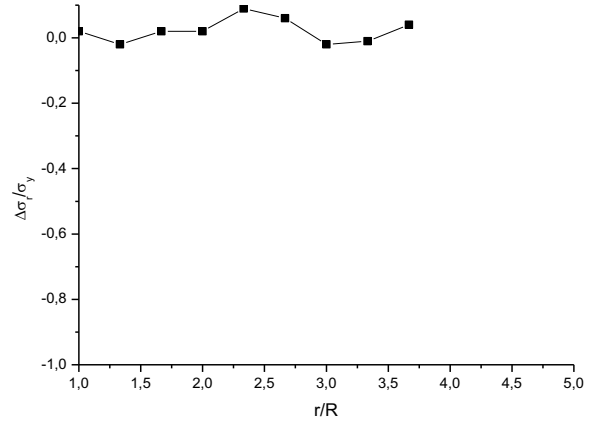

Fig. 4. The radial stresses increment $\Delta\sigma_r$ on the surface of the specimen on the side of it with machined rivet head (small specimen riveted manually: M3).

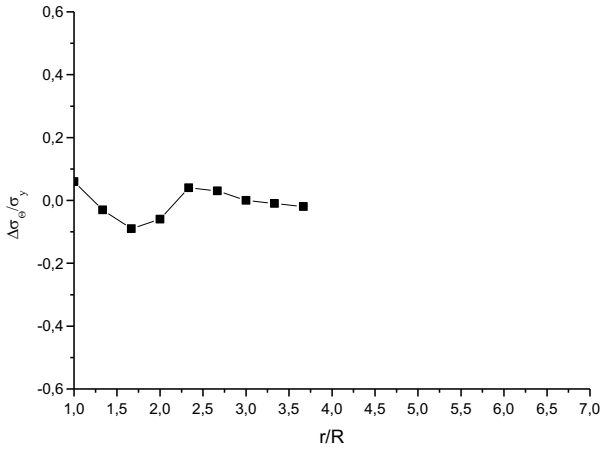

Fig. 5. The tangential stresses increment $\Delta\sigma_\theta$ on the surface of the specimen on the side with the machined rivet head (small specimen riveted with press: P1).

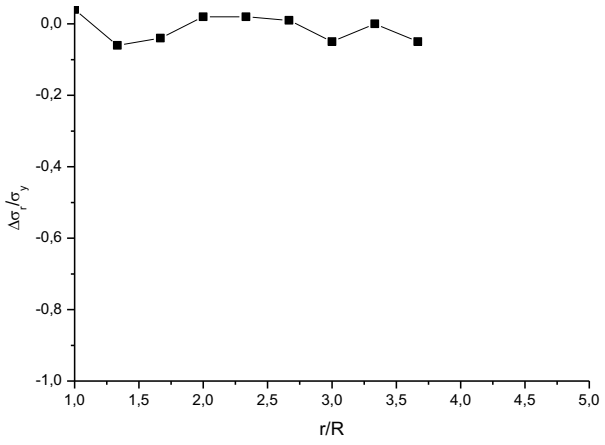

Fig. 6. The radial stress increment $\Delta\sigma_r$ on the surface of the specimen on the side with the machined rivet head (small specimen riveted with press: P1).

The comparison of the graphs presented above and the results obtained by R.P.G. Müller leads to the conclusion that the character of graphs obtained during the residual stresses measurement is inconsistent in each case.

The lack of consistency between the results of stress measurements and the FEM analysis forced the authors to analyze the measurement method and to improve it. It was stated that the reason for the error in stress measurement was the anodized layer and the cladding so it was necessary to work out the method of removing those layers to obtain more reliable results. The additional aim of preparing this type of specimen was to work out the method of removing the formed rivet head. To check if the applied treatment hasn't changed the stress state, measurements were performed on rivet wire specimens, after different kinds of treatments. The results of stress measurements on those samples are listed below:

Table 1. Results of the measurements on 3.5 mm diameter rivets, phi=0° corresponds to tangential direction and phi=90° to axial direction.

Rivet	Stress phi=0° Tangential direction		Stress phi=90° Axial direction		FWHM phi=0°	FWHM phi=90°
no	MPa	±MPa	MPa	±MPa	°	°
1	-63	4	-50	5	1.43	1.46
2	-69	3	-51	4	1.48	1.47
3	-28	3	-41	3	1.49	1.48
4	-38	3	-36	5	1.47	1.45
5	-39	5	-44	2	1.43	1.43
6	-3	3	-36	5	1.42	1.45

Table 2. Results of the measurements on 5 mm diameter rivets, phi=0° corresponds to tangential direction and phi=90° to axial direction.

Rivet	Stress phi=0° Tangential direction		Stress phi=90° Axial direction		FWHM phi=0°	FWHM phi=90°
no	MPa	±MPa	MPa	±MPa	°	°
1	-56	4	-49	6	1.44	1.45
2	-76	5	-68	3	1.46	1.46
3	-68	2	-61	5	1.47	1.47
4	-52	10	-58	6	1.43	1.44
5	15	3	-15	5	1.47	1.45
6	-6	4	-11	8	1.41	1.41

The surface layers of the specimens were removed with 6 different types of treatment. The removed layers were thick enough and the treatment of step 5 and 6 gentle enough to uncover the core material of the wire without changing its stress state.

Specimen of plate with three areas

Photo 3. Plate with three different areas. Directions of measured stresses.

The measurements on those three areas were performed before the application of any additional treatment (depth=0,000) and after removing a few microns of the surface layer by electropolishing. The aim of applying the additional treatment was to remove contamination of the specimen surface.

Table 3. Residual stress values on point 1.

Plate	Stress phi=0°		Stress phi=90°		FWHM phi=0°	FWHM phi=90°
Depth	MPa	±MPa	MPa	±MPa	°	°
0,000	-24	7	6	10	1,30	1,31
0,006	-55	5	-25	10	1,34	1,34

Table 4. Residual stress values on point 2.

Plate	Stress phi=0°		Stress phi=90°		FWHM phi=0°	FWHM phi=90°
Depth	MPa	±MPa	MPa	±MPa	°	°
0,000	-35	5	-68	5	1,31	1,32
0,005	-35	5	-54	5	1,34	1,34
0,008	-53	7	-61	8	1,34	1,35

Table 5. Residual stress values on point 3.

Plate	Stress phi=0°		Stress phi=90°		FWHM phi=0°	FWHM phi=90°
Depth	MPa	±MPa	MPa	±MPa	°	°
0,000	-53	4	-54	3	1,33	1,33
0,005	-45	3	-60	5	1,31	1,31

The difference between the results obtained for area no. 1 before applying the electropolishing and after removing 6 microns of the surface layer was caused by a different number of grains of aluminium participating in diffraction. The X-ray penetration depth is about 13 microns and the anodized layer thickness is about 7 microns. After removing 6 microns of the surface layer the measurement was performed almost only in the cladding layer.

CONCLUSIONS

The stress measurements around the rivets were not satisfactory enough. It was necessary to work out a method of removing the anodized layer and cladding to allow the stress measurements in the core material and compare them with the FEM analysis results.

1. Muller, R. P. G., *An Experimental and Analytical Investigation on the Fatigue Behavior of Fuselage Riveted Lap Joints*, Ph. D. Thesis, Delft University of Technology, The Netherlands, 1995, p.161.
2. Hakanen M., *Institute of Aviation – XRD measurements on riveted samples*, non published report No #699, Stresstech Oy, Vaajakoski 2007.
3. Hakanen M., *Institute of Aviation – Residual stress on rivets*, non published report No #744, Stresstech Oy, Vaajakoski 200.
4. Cullity B.D. *Podstawy dyfrakcji promieni rentgenowskich*, Państwowe Wydawnictwo Naukowe, wyd. I, Warszawa 1964.
5. ASM Handbook, Volume 9: *Metallography and Microstructures 2004.*
6. ASM Handbook, Volume 2:0 *Properties and selection: Nonferrous Alloys and Special-Purpose Materials.*
7. Industrial standard of Soviet Union, *Mushroom head rivets with compensator*, No. OST 1 34040-79.
8. Internat standard of PZL Mielec, *Countersunk rivet,* No. ANU 0301.

5.3 An Experimental Investigation on the Fatigue Performance of Riveted Lap Joints

(Małgorzata Skorupa - AGH University of Science & Technology, Kraków)

The results of an experimental investigation of the influence of various factors on the fatigue behaviour of riveted lap joints are presented. The variables considered are the squeeze force, the fastener type and the material. Also, the effect of a staggered sheet thickness in the overlap region is studied.

The constant amplitude fatigue tests were carried out on lap joint specimens with three rows of rivets installed under load control. The 2mm thick sheet material was a Russian Al alloy D16Cz in the clad condition which, as shown elsewhere [1], is similar to the 2024-T3 Alclad regarding its chemical composition, mechanical properties and the fatigue crack growth behaviour. The round head rivets and the so called rivets with compensators according to the Russian standard were used. The compensator is a small protrusion on the mushroom rivet head. For both types of rivets the ratio of the machined head diameter to the rivet shank diameter is about 2. Two Al alloy rivet materials used in the Polish aircraft industry were considered, namely PA24 and PA25 with the minimum shear strength of 185 MPa and 240 MPa respectively. The rivets can be installed in the as received condition. The tensile and compressive tests on the rivet wire have revealed that PA24 is similar to the Western AD rivet material. This was also confirmed by the measurement results on the driven head dimensions (D - diameter, H - height) versus the rivet squeeze force (F_{sq}), which coincided with the data reported for the AD rivets [2]. For PA25, the measured D vs. F_{sq} and H vs. F_{sq} data points fell respectively below and above the results for the Western rivets. In the present investigation, the round head rivets were of the PA24 alloy whilst both alloys were used for the rivets with compensators. The rivet shank diameter for all rivets was D_o=5 mm.

The effect of the rivet type and material was studied in the fatigue test series performed at the stress ratio R=0.1 and the maximum nominal stress S_{max}=120 MPa for D/D_o ranging from 1.3 to 1.6. Consistent with the literature data, e.g. [3], the fatigue lives (N_f) of the specimens joined using the rivets of the PA24 alloy increased considerably with increasing the D/D_o ratio, i.e. with elevating the F_{sq} level. The endurances for the rivets with compensators of PA24 were always longer than for the round head rivets. The joints with the PA25 rivets are superior to the others only at D/D_o values below 1.5. High F_{sq} values required to obtain larger head diameters for the PA25 material caused cracking of the driven rivet heads, which adversely affects the joint fatigue properties. In all cases, the fatigue fracture occurred at one of the outer rivet rows and the cracks initiated on the faying surface from or near the rivet holes. At a given D/D_o value, the crack nucleation site was always found to be more shifted from the rivet hole for a rivet with the compensator than for a round head rivet. The latter behaviour can be explained by a larger hole expansion promoted by the compensator.

In order to improve the fatigue quality of a lap joint Schijve proposed to stagger the sheet thickness within the overlap region for a joint with three rivet rows [4]. The concept is intended to provide for high stresses in the outer rivet rows by both reducing the secondary bending and lowering the load transmission through these rows. To verify the utility of the staggered thickness configuration the constant amplitude fatigue tests at R=0.1 have been carried out on three specimen series with the PA24 round head rivets shown in fig. 1a and b. For the staggered thickness geometry with p_s=1.5p the weight of the joint is the same as for the standard configuration. In order that the ”pure” effect of the joint geometry should be extracted in the tests, the D/D_o ratio of 1.3 has

been chosen. It was the highest value at which the crack initiation occurred still at the rivet hole edge. The fatigue test results shown in fig. 1c indicate the beneficial influence of the thickness staggering, especially for the larger rivetrow spacing. Though the percentage gain in the fatigue life decreases at the lower stress levels, still a considerable life increase of nearly 125 kcycles compared to the standard joint is observed at S_{max}=80 MPa for the staggered thickness configuration with p_s=1.5p.

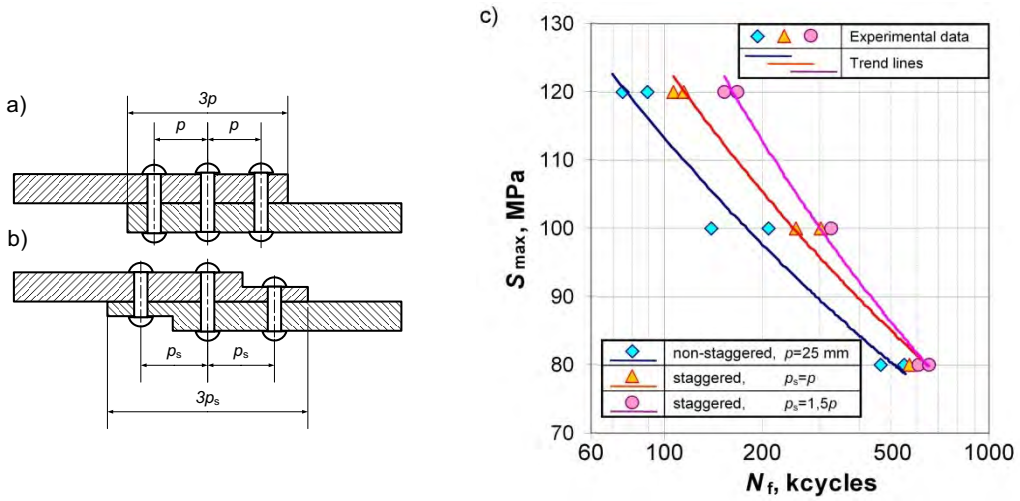

Fig. 1. Influence of a staggered overlap on the fatigue life of the riveted lap joint specimens: (a) standard configuration; (b) staggered thickness configuration; (c) S-N test data.

References

[1] Schijve J., Skorupa M., Skorupa A., Machniewicz T. and Gruszczyński P. Int. J. Fatigue 26 (2006), 1-15.

[2] Rijck de J.J.M. PhD thesis, Delft University of Technology, Delft, 2005.

[3] Müller R.P.G. PhD thesis, Delft University of Technology, Delft, 1995.

[4] Schijve J. Doc. B2-06-02. Delft University of Technology, Delft, 2006.

5.4 Fatigue Damage of Rivet Joints in the Condition of Stable Cyclic Load

(Volodymyr Hutsaylyuk - Military University of Technology, Warsaw)

The riveted joints are the critical areas of an aircraft structure. Exploitation loads lead to fatigue processes and aging of material, structural damage and defect accumulation, both at micro and at macro levels.

Therefore, to evaluate actual state of the structure as a whole, or a given element, there is a need to consider the riveted joints, paying special attention to its component elements.

The problem consists in damage beginning to accumulate under the rivet's head, in the area inaccessible for visual control (fig.1). At the initial stage of crack propagation, cracks grow in the body of the sheet without appearing to the surface. Damage in joints becomes visible only after a crack appears on the surface and reaches the size accessible for visual control. At the same time crack propagation into depth of the sheet is practically uncontrollable and may even reach up to 70% of the sheet thickness. Since a joint is usually created by a row of rivets, the moment of cracks creation on the surface might be critical for structure durability, since cross section is weakened due to crack propagation into depth of the sheet. Therefore, consideration of the initiation moment and primary crack propagation is an important part of prediction of remaining service life of joint and entire construction.

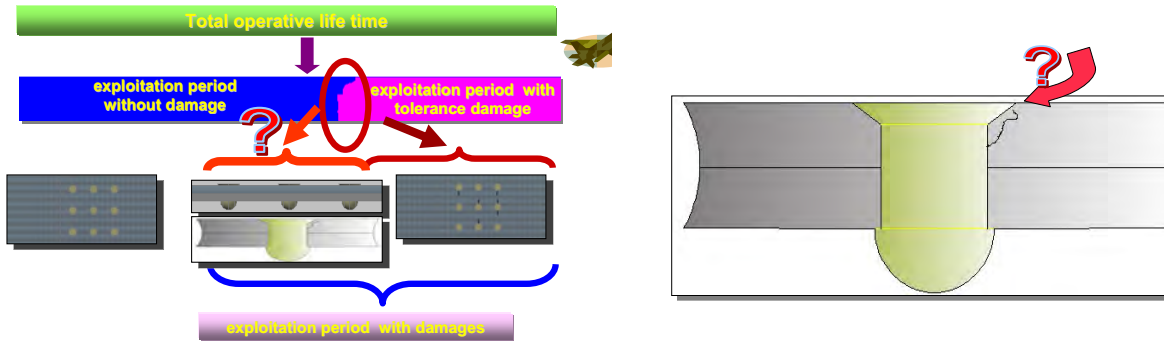

a b

Fig. 1 Schema of fatigue defects accumulations during exploitation term (a) and propagation of a primary short crack (b)

An equally important task is to determine initial fatigue defect in the form of a short crack, which initiates under the head of a rivet in main material of aluminium sheet and is inexccessible for visual observation. In this case the problem consists the necessity of using corresponding non-destructive methods of control which allow detecting damage and controlling its parameters.

It is understandable that from the moment of initiation of short crack (accumulation of critical mass of damage) to the moment of crack appearance on the surface all main fracture processes are being completed at micro level

The goal of this work was an attempt to work out methods for determination of initial damage of material, which could be accepted as primary for defining a period of exploitation with damage up to the moment of its visualisation. An equally important goal was research of micro mechanisms of fracture at the initiation stage, propagation of crack at the forming stage of macro crack and transition to the stage of final failure.

The aluminium alloy 2023-T3 was used in this tests. The specimens for testing were made from sheet and were cut from double-sided lamellar aluminum in direction of rolling. For testing three types of unified specimens were used (fig. 2).

Research was realized on testing machine «Instron» (fig. 3) at cyclical load of stable amplitude $\Delta\sigma$=100MPa, at frequency of 15 Hz and coefficient of asymmetry R=0.15, 0.3, 0.5.

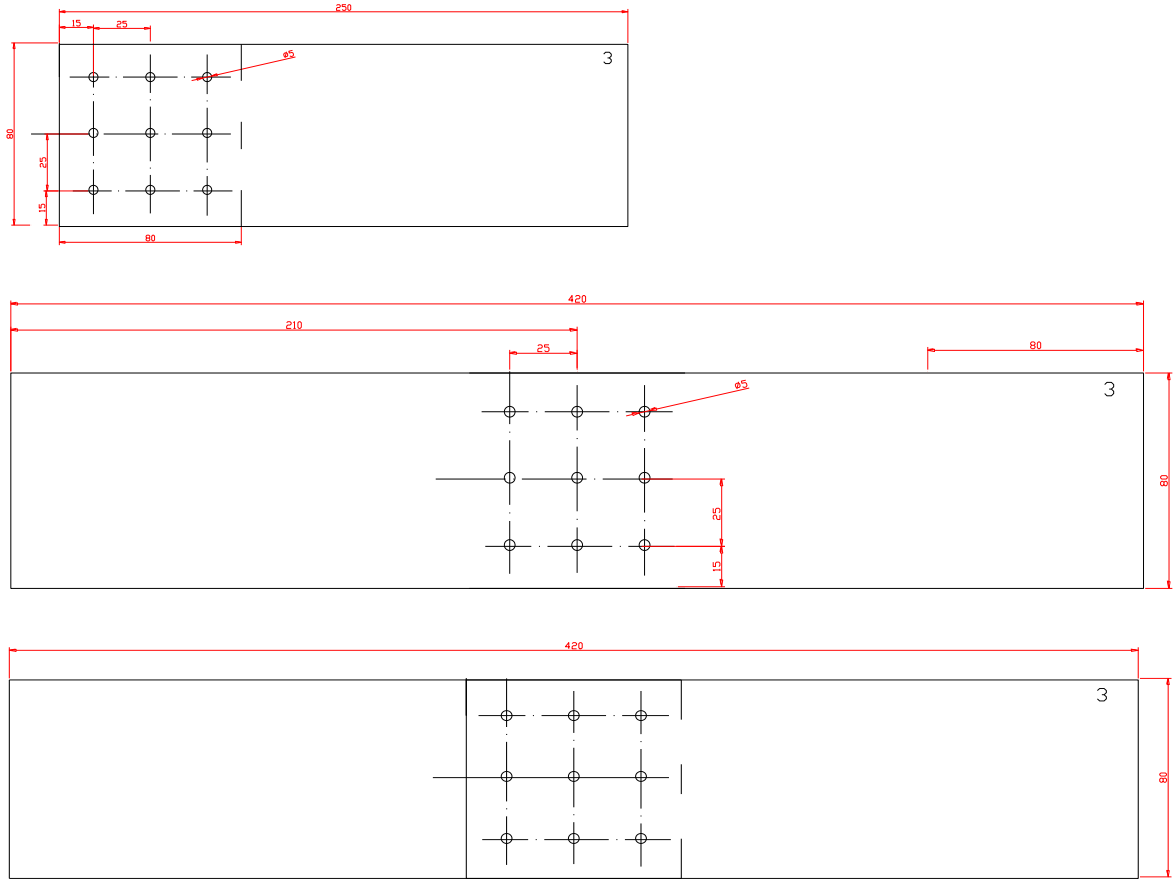

Fig. 2. Specimens for testing

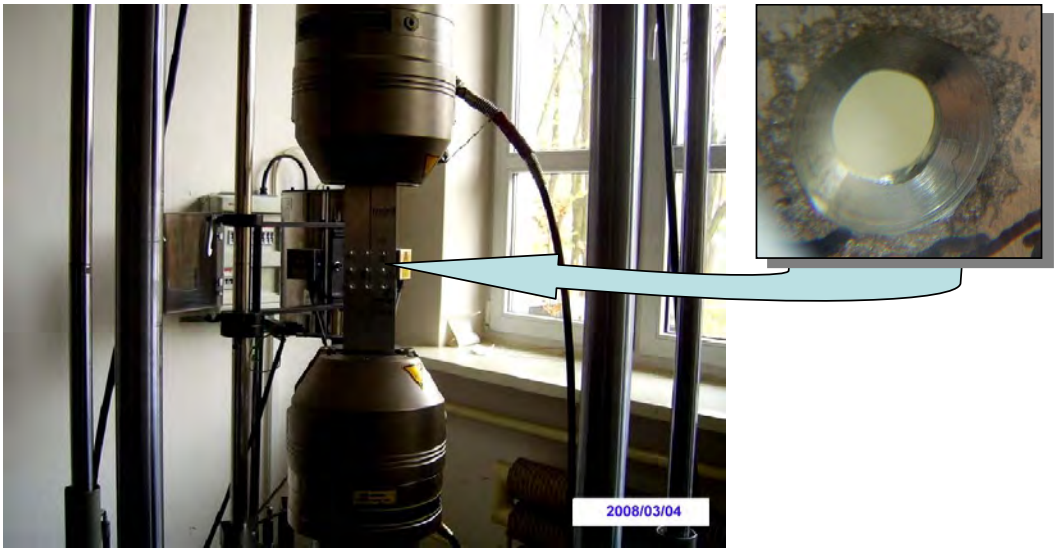

Fig. 3 Testing machine

During testing the control was performed visually and by use of optical microscope at 25 x magnification.

For the control of material damage the vortex-current defectoscope BD 3-71 with a sensor of a converting type PN-12 MDF 01 was used.

Conclusions

1. On the basis of conducted research the method of determining initial micro-damage of elements in rivet joint using the vortex-current detector was developed.
2. The micromechanism of fracture of aluminum alloy 2024-T3 in conditions of steady-amplitude cyclic load was analyzed.
3. The influence of microstructural changes must be considered during design of any model for prediction of crack propagation, either at the stage of short or at the stage of long crack, especially when predicting or estimating remaining service life.

6. OTHER RELEVANT WORKS

6.1 Experimental crack propagation analysis of the compressor blades working in high cycle fatigue condition.

(Lucjan Witek – Rzeszów University of Technology, Rzeszów)

This work was concerned with the experimental vibration tests of the helicopter turbo-engine compressor blades. The blades were tested in high cycle fatigue (vibration) condition. By specifying only one load component and analysis of experimental and numerical results, the complex fatigue failure process of compressor blades can be better understood. The additional goal of this investigation was to provide an answer to the question: how fast the crack can propagate inside the structure?

The blades used in experimental fatigue tests were withdrawn from use after technical inspection of the engine (fig. 1). Experimental investigations were performed at Research and Development Laboratory for Aerospace Materials of Rzeszów University of Technology.

Fig. 1. Blades of the I-st stage compressor

Before fatigue testing, each blade was horizontally mounted on the head of vibrator (fig. 2). After that, the head with the blade were subjected to sinusoidal (harmonic) vibration. During the test, both the amplitude of vibration of the blade tip and the size (or apperance) of the crack were periodically monitored. The blade with crack initiation zone and the crack detected during the fatigue test are presented in fig. 3.

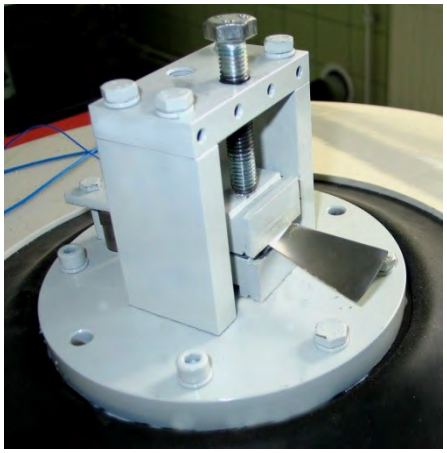

Fig. 2. The blade mounted on the head of the vibrator.

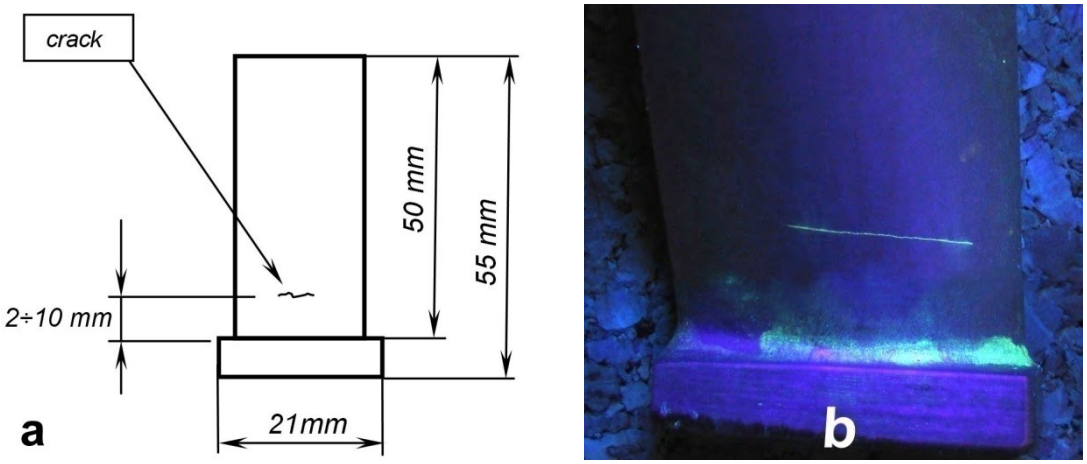

Fig. 3. The compressor first stage blade with the crack location (a) and view of the crack in UV light (b).

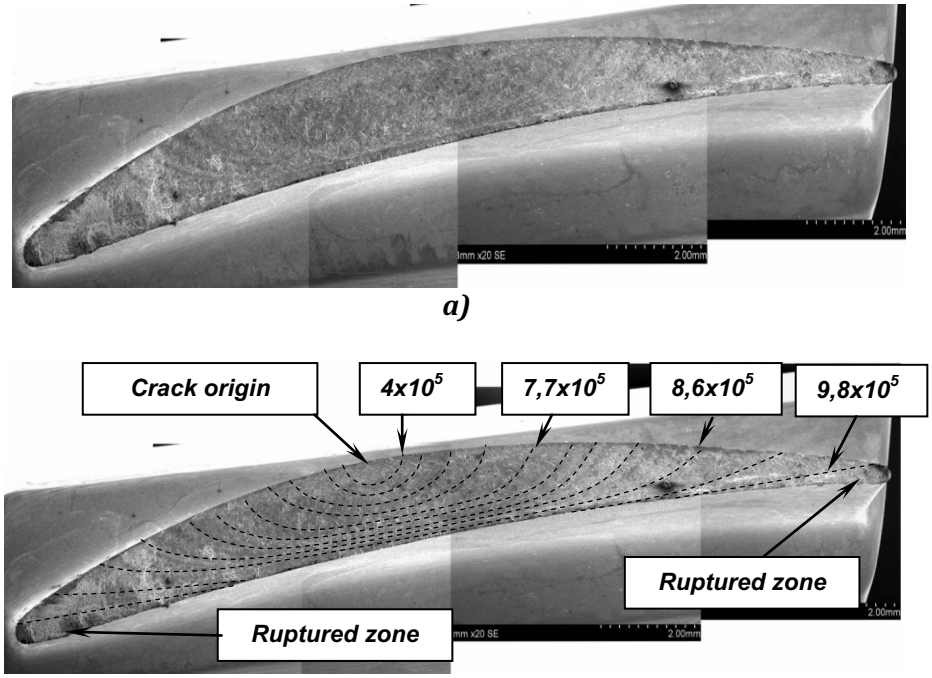

a)

Fig. 4. View of damaged blade (a). Fracture with marked beach marks, created by different numbers of cycles (b), blade no. 1.

The results presented in fig. 4÷7 and Tab. 1 were obtained from tests in which the intensity of vibration was defined as 12g (for blades no. 1, 2 and 3). The fractured blade 1 is shown in fig. 4. The crack was initiated on the convex surface of the profile, about 6 mm above the blade locking piece. The crack origin zone was not covered by corrosion products.

The control parameters of the vibration system and results obtained for blade 1 are shown in Tab. 1. As seen from this table, the resonant frequency for the blade is 774 Hz, and from this frequency the test was started. After 4×10^5 total number of cycles, the amplitude of the blade tip decreased from 2,5 mm to 2,25 mm. Under cracking, the bending stiffness of the blade is decreases. This information is very important, because the decrease of amplitude at constant intensity of excitation is often related to start of the crack initiation process. In this case, 1 mm long crack was detected. From the $6{,}76\times10^5$ number of cycles, the excitation frequency decreased at the rate from 0.2 to

1 Hz/sek. The crack length in function of the total number of cycles (crack growth plot), obtained for blade 1 is presented in fig. 5.

Table 1. Control parameters of the vibration system and results obtained for blade no. 1.

Initial frequency	Final frequency	Rate of change of frequency	Partial no. of cycles	Total no. of cycles	Crack length	Amplitude of crack tip
F_{init} [Hz]	F_{fin} [Hz]	df/dt [Hz/sek]	N_{part} x 10^5	N x 10^5	a [mm]	A [mm]
774	774	0	0	0,00	0	2,50
774	774	0	1	1,00	0	2,50
774	774	0	1	2,00	0	2,50
774	774	0	1	3,00	0	2,47
774	774	0	1	4,00	1	2,25
774	774	0	1	5,00	2,5	1,75
774	774	0	1	6,00	4,5	1,35
770	750	0,2	0,76	6,76	6,3	1,20
750	725	0,2	0,92	7,68	9	1,10
725	700	0,2	0,89	8,57	12	1,05
700	600	1	0,65	9,22	15	1,03
600	500	1	0,55	9,77	19	1,03

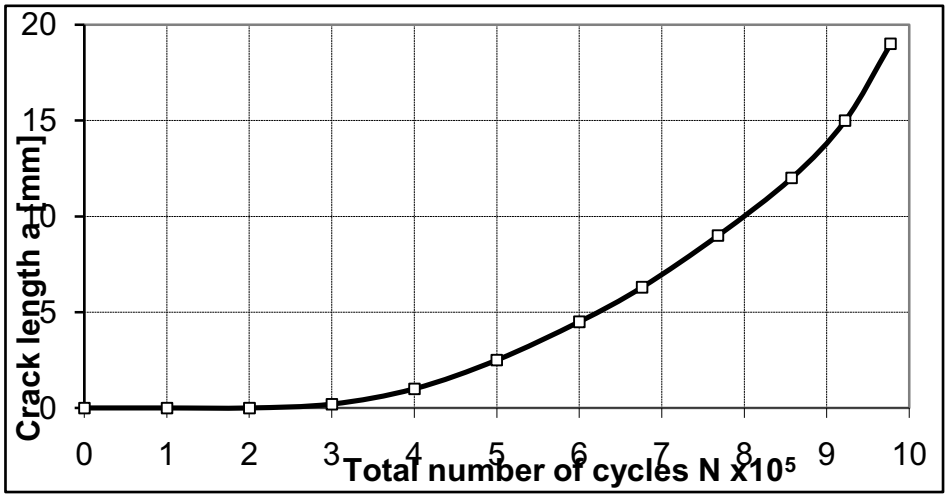

Fig. 5. Crack length in function of total number of cycles for the compressor I-st stage blade (intensity of vibration 12g, blade no. 1).

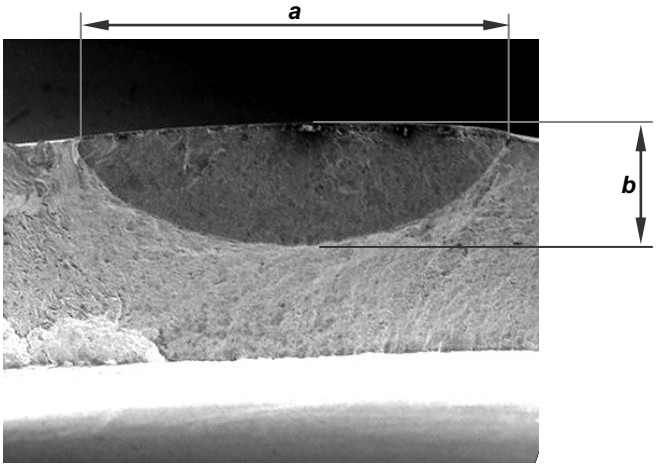

Fig. 6. Shape of the crack front just after crack initiation (blade no. 2).

The fatigue test for blade number 1 was conducted in short time and the crack was propagated in non-corrosive environment, thus the beach marks presented in fig. 4a are not well visible, especially around the crack origin zone. In order to better determine crack front shape at the early stage of fracture, blade no. 2 was vibrated only to the first crack detection. Next, the blade was statically tensioned and ruptured with the use of the testing machine.

Fig. 6 is a magnified view of the fractured surface. As seen from this figure, the crack front in the early stage of fatigue moves intensively inside the structure. The depth of the crack (dimension b) is about 50% of the total blade thickness. The fatigue fracture area is dark grey.

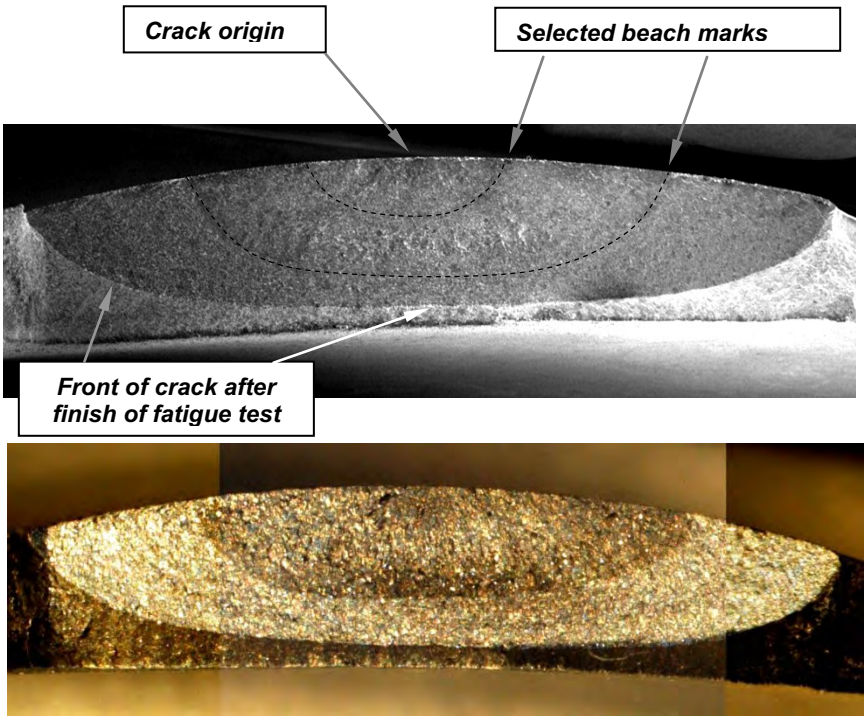

Rys. 7. Shape of the crack front in the advanced phase of fatigue, after about 8×10^5 number of cycles, visible with the use of scaning (a) and optical (b) microscope (blade no. 3).

The blade number 3 was vibrated as long as the fatigue crack length (dimension a) was about 10 mm. Next, the blade was statically ruptured with the use of the testing machine. The shape of the crack in the advanced phase of growth is presented in fig. 7. As seen in this figure, the crack in the advanced phase of growth propagated quickly in the horizontal direction.

In this work, the results for only three out of ten blades were described in detail. The damage schemes of the remaining blades are similar to those presented in fig. 4. The cracks were initiated on the convex surface of profile, from 2 mm to 10 mm above the blade locking piece (fig. 8). The crack origin zones were not covered by corrosion products.

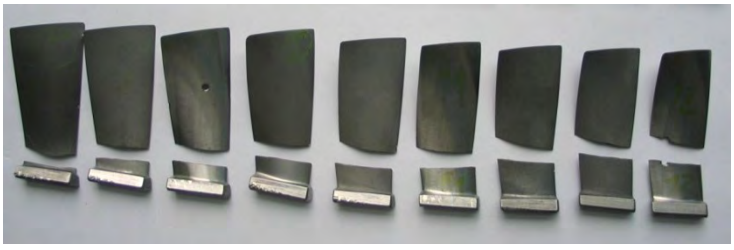

Fig. 8. Ruptured blades of the I-st stage of the compressor after investigations.

The computations for the blade, working in the vibration conditions, were performed for the analysis of stress state occurring during the blade resonance. In this analysis, the first mode of transverse vibration was considered. Parametric geometry models of blade were made using the MSC-Patran program (fig. 9). The ABAQUS v. 6.7 program was used for stress analysis.

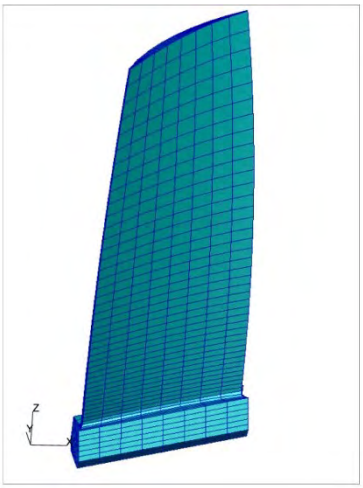

Fig. 9 Finite element model of the compressor blade.

The compressor blade is made from EI-736 material. The yield point of EI-736 alloy in temperature 0^0C is 820 MPa, while the UTS (ultimate tensile strength) is 969 MPa. The analysis presented in this paper was performed for linear-elastic blade materials.

The blade under vibration is being periodically bent to the left and right sides (fig.10). Because of the fact that the cross-section of the blade is non-symmetric, the stress levels under left and right deflection of the blade will be quite different. In description of figures and results, the information about blade deflection will be given.

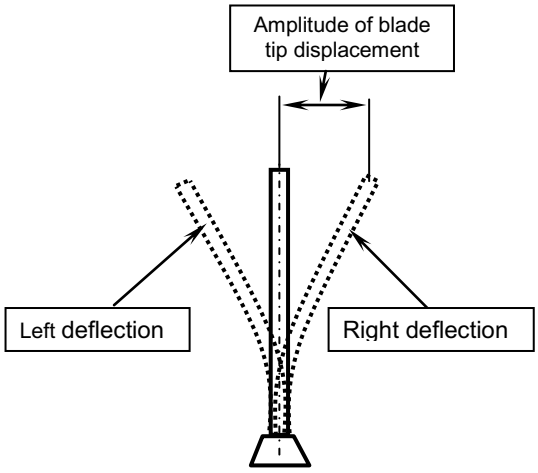

Fig.10. Passing positions of blade under vibration.

Fig. 11 shows that the tensile stress on the convex surface of blade, where the cracks appeared, achieves 622-1011 MPa (for the right deflection of the blade). The maximum stress region (1088 MPa) is located about 1 mm above the blade locking piece, on the central part of the convex surface (fig. 12a). Near the neutral axis of the blade cross-section, the tensile stress decreases to 0 MPa. Between the maximum stress region and the neutral axis, the high gradient of stresses is observed. During the left deflection, the maximum tensile stress region (934 MPa) is located near the attack edge of the blade (fig. 12b).

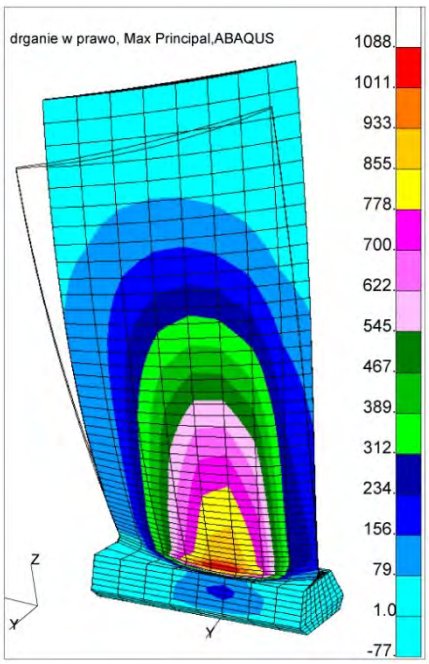

Fig. 11. Maximum principal stress distribution for the blade during resonance (mode I, transverse vibrations, amplitude of the blade tip: 2,5 mm, the right deflection of the blade.

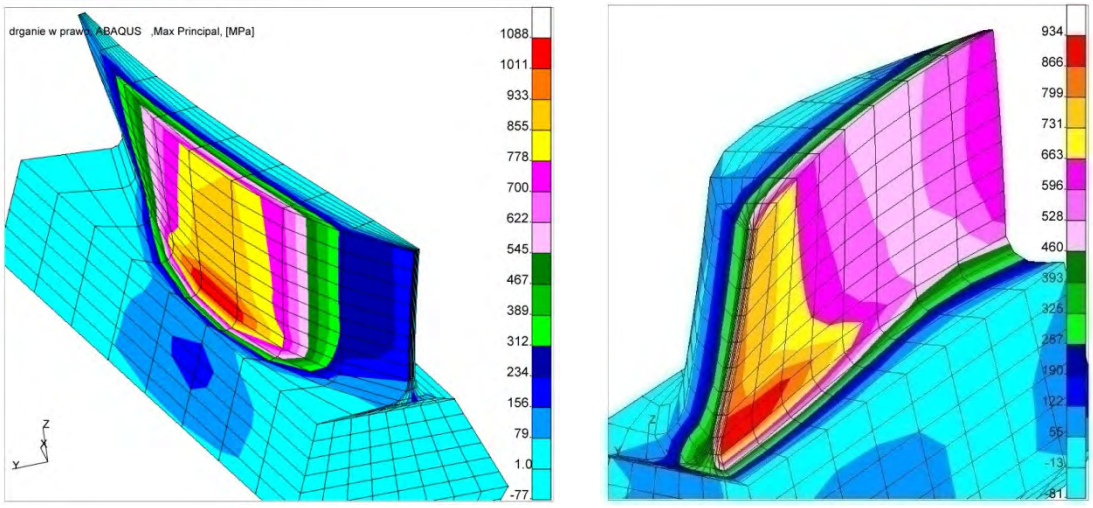

Fig. 12. Maximum principal stress distribution during resonance (mode I, transverse vibrations, amplitude of the blade tip: 2,5 mm,). Cross-section in the crack zone before the crack initiation. Right (a) and left (b) deflection of the blade.

The following conclusions were formulated:

1. The total fatigue life of the compressor blade was equal $9{,}97\times10^5$ number of load cycles. A relatively large amplitude of vibration (2,5 mm at beginning of test and 1 mm at finish) caused that high crack growth rate was observed, especially when crack size (fig 6, 7) was bigger then 10 mm.
2. The crack origin zone was not covered by corrosion products.

3. The analysis of numerical results showed that the main reason for fatigue cracks appearing was the high stress occurring during the blade resonance. Moreover, in the cross-section of the blade, the high stress gradient was observed.
4. The transverse vibrations can be very dangerous for the compressor blades because of the high stress occurring during the blade resonance. In consequence, the crack can rapidly grow to the critical size leading to engine failure.

Acknowledgements

This work was supported by Polish Ministry of Science and Higher Education (Project no. N N 504 346736). The author would like to thank Prof. J Sieniawski and K. Kubiak-D.Sc. for the possibility of performing the fatigue investigations at Research and Development Laboratory for Aerospace Materials of Rzeszów University of Technology.

6.2 Thermal Fatigue Problems of Turbine Casing

(Lucjan Witek – Rzeszów University of Technology, Rzeszów)

This work was concerned with the numerical stress and strain analysis of an aero-engine turbine casing (part of engine used for drive of PZL-W3 “Falcon” helicopter). In this engine some problems related to cracks appearance and premature fatigue fracture of the connection between deflectors and outer cylindrical casing occurred (fig. 1-4). The experimental explanation of this problem is not easy. An answer to the question about fracture of casing can be given by the numerical stress analysis.

Fig 1. View of a turbine casing for the small helicopter turbo-engine.

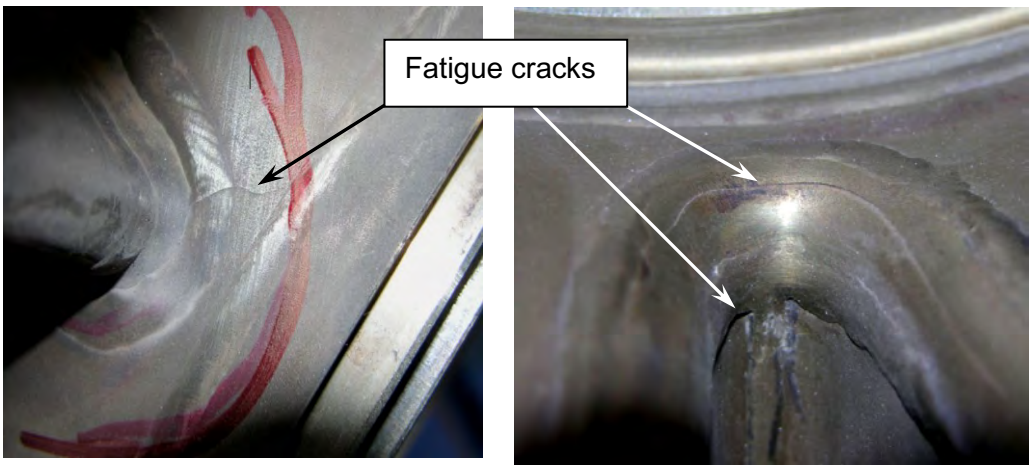

Fig. 2. Fatigue cracks detected during the engine inspection.

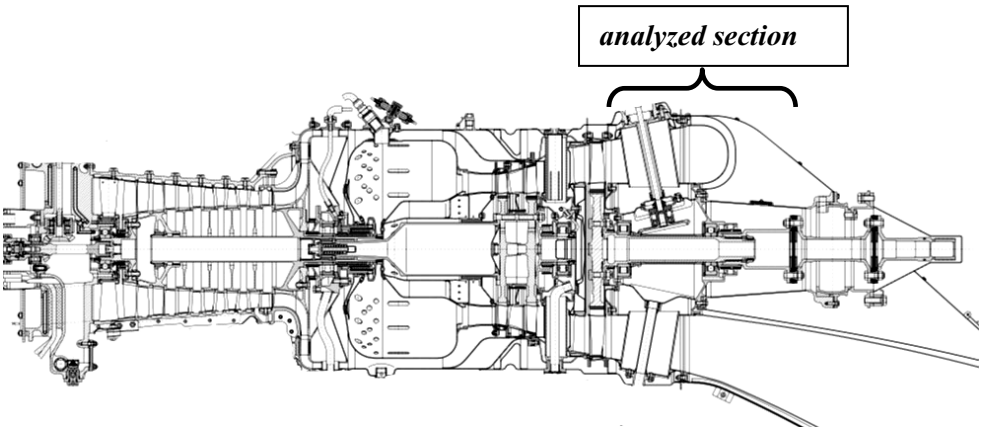

Fig. 3. A cross-section of the engine.

The component of the engine (turbine casing) in which the fatigue cracks were detected is located between the power turbine section and the exhaust manifold/transmission box section (fig. 3). All figures and tables presented in this work were published in the Diploma Thesis of the second researcher (D.M. Ngii, Rzeszow University of Technology, 2007).

The numerical model presented in fig. 4 consists of 12889 nodes, 12690 shell elements, 28 bar elements and 20 MPC's.

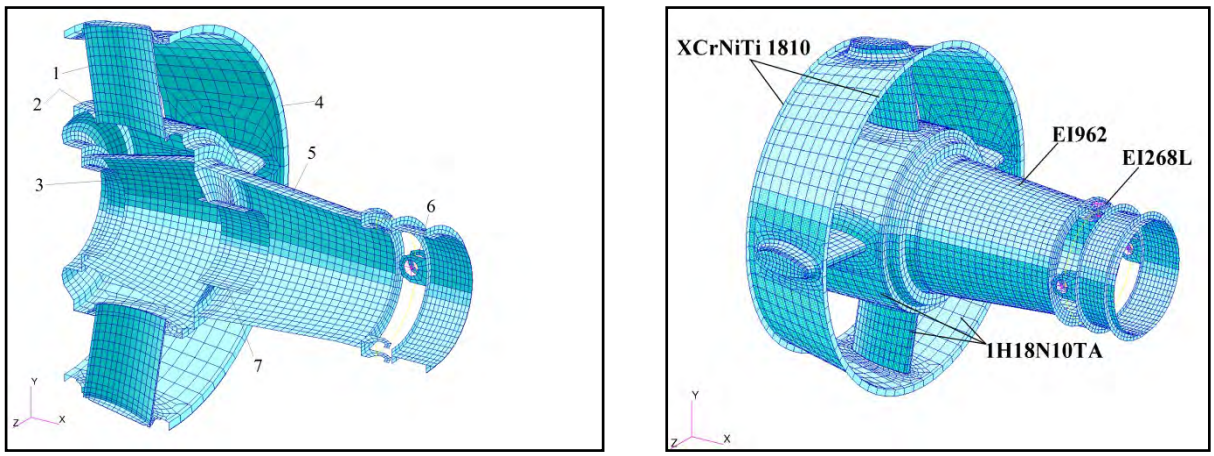

a) *b)*

Fig. 4. A longitudinal cross-section of the turbine casing (a) and materials used in different parts of the numerical model (b).

The turbine casing consists of the following parts (fig 4a):

1. Deflector.
2. Cylindrical casing.
3. Inner conical casing.
4. Flange.
5. Rear conical casing.
6. Universal couple joint.
7. Bearing casing.

The turbine casing was made of four different types of alloys which are presented in fig. 4b. In the numerical model the appropriate material constants (i.e. Young modulus in function of temperature) were defined for modeling of the mentioned alloys. All materials are defined as linear-elastic.

The stresses occurring in the turbine casing arise owing to both the mechanical and thermal loads. Among the mechanical loads, the following forces can be distinguished: weight force (R_C), force related to bearing clearance (R_L), force related to gyroscopic moment (Rz), longitudinal force (R_W) and imbalance force (R_N). Values of these forces used in computations (Tab. 1), were defined on the basis of the technical project of the engine.

The mechanical forces were defined as a continuous load (with use of the MPC elements), imposed on the surface of the model where the bearings are located.

Table 1. Mechanical forces acting on the turbine casing (transferred from shaft, for first load case).

Force	**R_{IV} [N]**	**R_V [N]**
Weight RC	98.2	49.1
Bearing clearance RL	982	982
Gyroscopic Rz	491	491
Longitudinal Rw	-	1178.4
Imbalance/ Geometrical irregularity RN	687.4	196.4

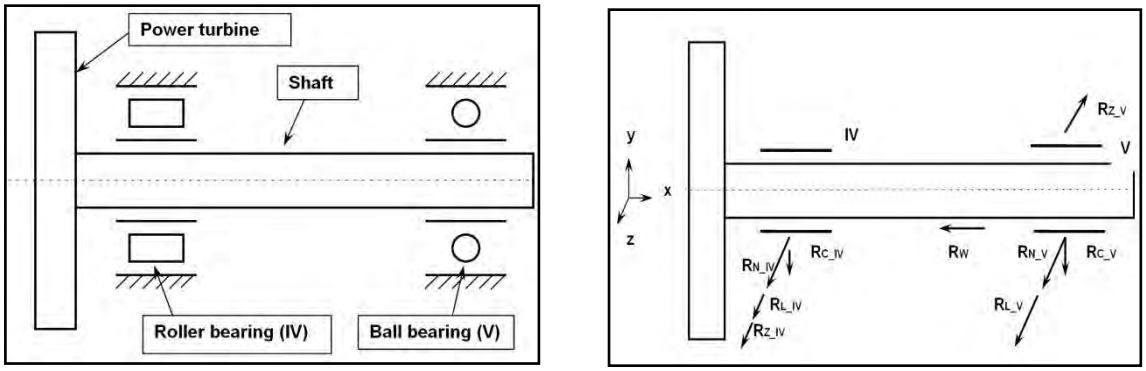

a) ***b)***

Fig. 5. Location of the bearings inside the casing (a) and forces acting from the shaft on the turbine casing for the specified load condition (b).

In this analysis, the thermal load was also considered. The temperature field was defined as a two parametric function in the cylindrical coordinates. The temperature values, obtained from the technical project of the engine are presented in fig. 6.

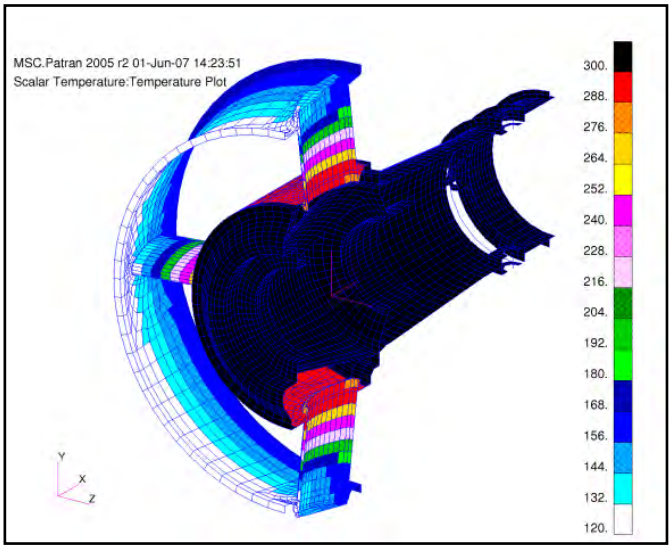

Fig. 6. Temperature field defined for the numerical model of the casing (Celsius scale).

The MARC-2005 program was used for stress analysis of the engine casing. For all results, Megapascal (MPa) units were used to describe the fields of stresses.

Fig. 7 shows that the tensile stress in the critical region where the cracks appeared (connection between deflectors and the outer cylindrical casing), achieves 188 MPa (fig. 7). Under loading, the outer cylindrical part of casing is strongly distorted (Fig. 8). By specifying two load components, it was possible to estimate which load has more impact on the premature fatigue failure of the casing. As seen in fig. 9, the thermal stresses observed in the model are about twice as large as the mechanical stresses.

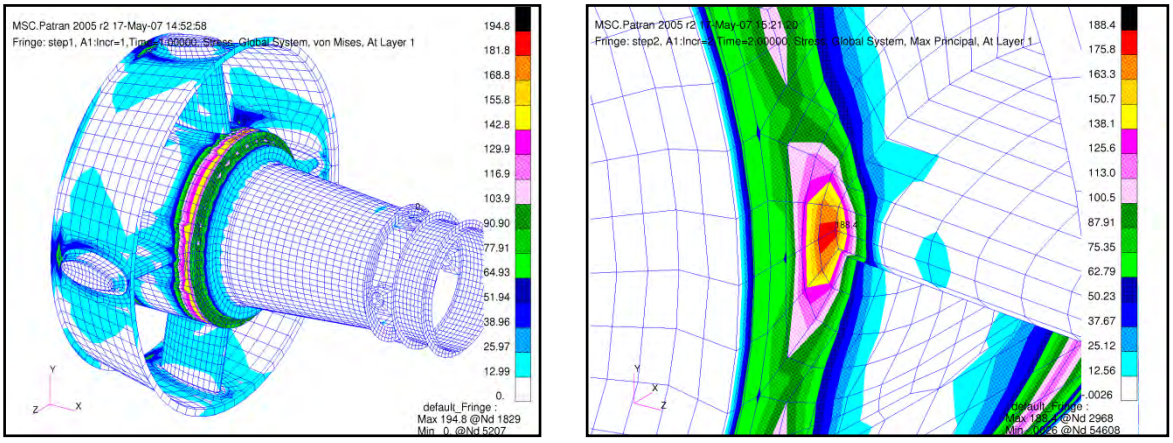

a) ***b)***

Fig. 7. Von Mises stress distribution for the casing (a) and maximum principal stress values in the critical region of the component (b).

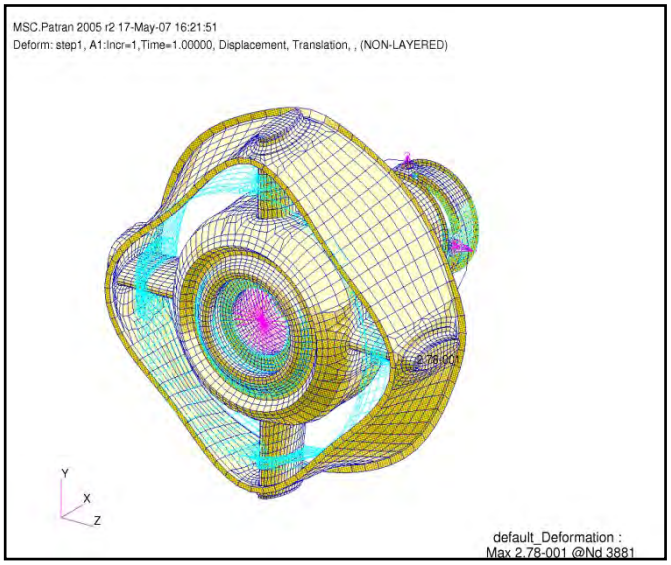

Fig.8. A visualization of the casing deformation (front view, scale of deformation 150:1)

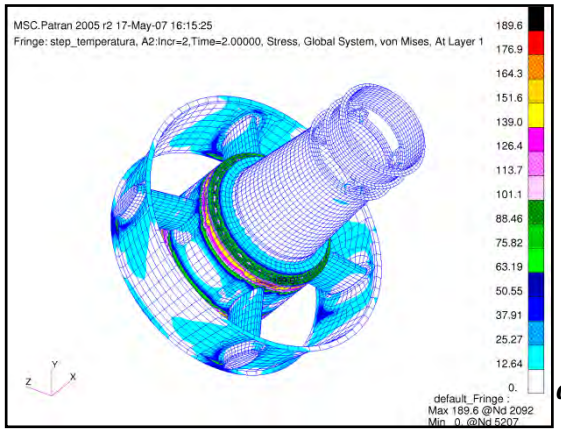

a)

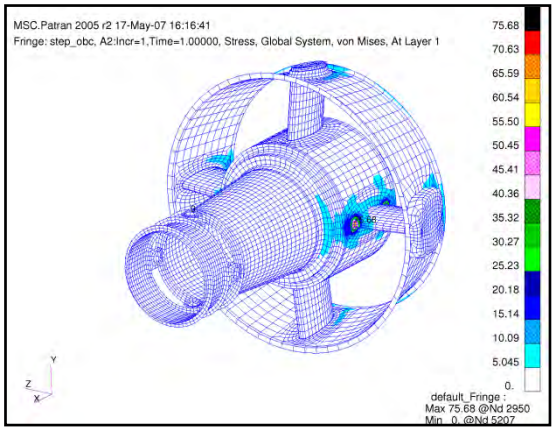

b)

Fig. 9. Von Mises stress resulting from thermal load (a) and mechanical load (b).

The following conclusions can be formulated:

1. The stress in the critical zone where the first fatigue crack occurs (fig. 7) was at about 180-190 MPa. This value is close to the yield stress of the material (220 MPa for temperature 200^{O}C). The cyclic variation of stress in this critical zone was the reason for fatigue crack arising.
2. The thermal stresses observed in the model were about twice as large as the mechanical stresses (fig. 9). Based on this information, the next conclusion is that low cycle thermal fatigue (LCTF) was the reason for premature fatigue failure of the analyzed engine casing.
3. It can also be concluded that the additional stresses due to vibrations of the engine were the reason for decreasing the fatigue life of the casing. However, the dynamic analysis was not performed in this work.